Journal of Controlled Release 376 (2024) 777–793

Contents lists available at ScienceDirect

Journal of Controlled Release

journal homepage: www.elsevier.com/locate/jconrel

Extracellular vesicles powered cancer immunotherapy: Targeted delivery of adenovirus-based cancer vaccine in humanized melanoma model

Sara Mathlouthi [a], Lukasz Kuryk [b], Marta Prygiel [b], Maria Giovanna Lupo [c], Aleksandra Anna Zasada [b], Cristiano Pesce [a], Nicola Ferri [c,d], Beate Rinner [e], Stefano Salmaso [a], Mariangela Garofalo [a,*]

[a] Department of Pharmaceutical and Pharmacological Sciences, University of Padua, Via F. Marzolo 5, 35131 Padua, Italy
[b] Department of Virology, National Institute of Public Health NIH - National Research Institute, Chocimska 24, 00-791 Warsaw, Poland
[c] Department of Medicine, University of Padova, Via Giustiniani 2, Padua 35131, Italy
[d] Veneto Institute of Molecular Medicine, Via Orus 2, 35131 Padua, Italy
[e] Division of Biomedical Research, Medical University of Graz, Roseggerweg 48, 8036 Graz, Austria

ARTICLE INFO

Keywords:
Oncolytic adenovirus
Extracellular vesicles
Melanoma
Immunotherapy
cancer vaccine
Targeted delivery

ABSTRACT

Malignant melanoma, a rapidly spreading form of skin cancer, is becoming more prevalent worldwide. While surgery is successful in treating early-stage melanoma, patients with advanced disease have only a 20 % chance of surviving beyond five years. Melanomas with mutations in the NRAS gene are characterized for a more aggressive tumor biology, poorer prognosis and shorter survival. Hence, new therapeutic strategies are needed, especially for this specific group of patients. Novel approaches, such as cancer vaccines, offer promising solutions by stimulating the anti-tumor immune response. Nevertheless, their clinical efficacy is still modest and more effective approaches are required. Herein, we propose the systemic administration of the adenovirus-based cancer vaccine complexed in extracellular vesicles (EVs) with the aim of achieving a targeted therapeutic effect. The vaccine was based on previously tested oncolytic adenovirus Ad5/3-D24-ICOSL-CD40L in combination with melanoma-specific antigens targeting NRAS mutations to enhance the anticancer effect. The antineoplastic properties of the oncolytic vaccine were evaluated in xenograft MUG Mel-2 melanoma BALB/c nude mice. Moreover, to mimic the tumor microenvironment, while investigating at the same time immune cell infiltration and drug penetration, we established a 3D co-culture model based on human NRAS mutated MUG Mel-2 spheroids and PBMCs (HLA matched), which displayed a synergistic effect when treated with the cancer vaccine compared to relative controls. Subsequently, we investigated the systemic delivery of the vaccine in EV formulations in a humanized NSG MUG Mel-2 melanoma mouse model. Our study provides a promising strategy for a tumor-targeted vaccine delivery by EVs, resulting in improved anticancer efficacy and increased infiltration of tumor-infiltrating lymphocytes. This study explores the potential of EVs for the selective delivery of cancer vaccines against malignancies, such as NRAS melanoma. Overall, this research could pave the way for applying autologous EVs as a safe and efficacious tool for targeted cancer therapy.

1. Introduction

Malignant melanoma is the deadliest form of skin cancer, and its incidence is increasing worldwide at a very fast rate [1]. Most patients receive their diagnosis during the initial stages of the disease, when treatment success rates are significantly higher; the 5-year survival is 98 % in stage IA and 70 % in stage IIC [2]. Nevertheless, advanced or metastatic cases are characterized by a high mortality rate; thus, their management is still a challenge for clinicians [3]. Genetic analyses conducted on the tumor tissue of patients affected by melanoma have shown that in approximately 20 % of cases a driver mutation is present in the NRAS gene, which therefore represents a potential therapeutic target in the treatment of this pathology [4]. Mutant NRAS melanomas are characterized by an aggressive tumor biology which could be attributed to the observation that such tumors tend to initiate the vertical growth phase earlier [5]. Moreover, NRAS mutant melanomas tend

* Corresponding author.
E-mail address: mariangela.garofalo@unipd.it (M. Garofalo).

https://doi.org/10.1016/j.jconrel.2024.10.057
Received 28 June 2024; Received in revised form 22 October 2024; Accepted 28 October 2024
Available online 1 November 2024

to be associated with higher rates of metastasis and poor overall survival [6]. To date, NRAS is still considered an undruggable target as no FDA-approved therapies have been forthcoming [3].

Cancer immunotherapy has revolutionized the approach to cancer treatment, aiming to enhance immune responses against tumors while minimizing off-target effects compared to conventional treatments [7], immunotherapeutic agents such as cancer vaccines are employed to activate or boost the immune system's ability to target cancer cells [8]. Peptide-based cancer vaccines for therapeutic purposes may direct the immune response to a specific target, nevertheless their limited clinical efficacy is mainly related to a lack of a proper adjuvant [9]. The next generation of cancer vaccine, based on the use of messenger RNA in cancer immunobiology is receiving increasing attention as mRNA can work as an effective vector for delivering therapeutic immune cancer epitopes [10]. However, this appealing technology is also limited by challenges, such as low stability against extracellular RNases, poor delivery efficiency to the target organs and cells, short circulatory half-life, and variable expression levels [11].

Therefore, while current immunotherapies with immune-checkpoint inhibitors may offer some hope, these are not mutation-specific, and up to 60 % of patients acquire resistance to the treatment and subsequent loss of response [12]. Therefore, the population affected by NRAS mutated melanomas needs new therapeutic approaches.

Oncolytic viruses, which are engineered to infect and kill cancer cells selectively [13,14], have been proposed as possible tool to treat cancer since they offer a versatile platform for immunotherapy, functioning as *in situ* vaccines [15,16] by inducing both oncolysis and specific adaptive antitumor immune responses, often $CD8^+$ T cell–mediated [17]. Moreover, they can be armed with immunomodulatory transgenes or used in combination with other immunotherapies enabling the release of immune factors and the direct targeting of tumor cells [18]. Nevertheless, despite promising achievements in preclinical studies, OV-based therapy faces some challenges that limit its application in the clinic due to low efficacy and production of anti-viral neutralizing antibodies [19]. The generation of anti-viral immunity is an important limitation that prevents efficient viral replication and spread in cancer cells when given systemically [20]. To overcome these hurdles, the intratumoral administration is preferred [19]. However, the OV-systemic administration route is preferable for treating patients, especially with no injectable lesions.

Taking the above into consideration, extracellular vesicles (EVs), which are naturally occurring nano-to-micron-sized delivery vehicles, have an appealing potential. They have been explored in the field of biomedicine due to their unique properties, including biocompatibility, cargo loading capacity and deep tissue penetration thus representing safe vehicles for tumor-selective delivery of anticancer agents [21–23]. Moreover, recent works provided compelling evidence for using cancer derived-EVs for the delivery of cancer viruses, such as oncolytic vectors [24], chemotherapeutics [23], and peptides [25].

Therefore, in this study, we set to investigate whether melanoma derived-EVs could be used for a systemic delivery of anticancer vaccines based on selected melanoma-derived epitopes (NRAS mutated melanoma antigens (ILDTAGREEY ($Q61R_{55–64}$), ILDTAGKEEY ($Q61K_{55–64}$), GLAPPQHLI ($P53_{187–195}$), SVYDFFVWL (TRP-$2_{180-188}$)) combined with previously tested oncolytic adenovirus [26]. Herein, by using an NRAS mutated human melanoma cell line grown in a humanized NSG CD34+ mouse model and a fluorescent dye to track EVs, we took advantage of *in vivo* and *ex vivo* imaging technologies to evaluate the biodistribution and the effects of EV-formulations carrying the cancer vaccine on the human immune system and anti-cancer effect.

We emphasise that an effective therapeutic strategy requires targeted delivery, coordinated destruction of cancer cells, activation of tumor-specific immunity and increased recognition of melanoma cells in primary tumors and distal metastases. Therefore, our research integrates available knowledge on melanoma antigens, vaccinology, oncolytic virotherapy and extracellular vesicles, which could be utilized to envision improved therapeutics with broader application and enhanced efficacy for melanoma patients.

We found that EVs enhanced the systemic delivery of the cancer vaccine, resulting in improved anti-cancer benefits and tumor-targeted delivery, which correlates with enhanced immune cell infiltration. Therefore, this approach could pave the way for a systemic administration of immunogenic vaccines in hard-to-inject melanoma.

2. Materials and methods

2.1. Cell lines, viruses and tumor epitopes

The study was conducted on a panel of melanoma cell lines (Table 1): human melanoma cell lines MUG Mel-2 (cellbankGraz) and A375 (ATCC, Manassa, VA), derived from skin lesions were cultured in RPMI 1640 media (Gibco Laboratories, CA, USA) supplemented with 1 % of penicillin/streptomycin (Gibco Laboratories, USA), 1 % L-glutamine (Gibco Laboratories, USA) and 10 % fetal bovine serum (FBS, Gibco Laboratories). Murine melanoma B16V cells (DSMZ, Germany) were cultured in DMEM low glucose medium (Sigma, Germany) supplemented with 1 % of penicillin/streptomycin (Gibco Laboratories, USA), 1 % L-glutamine (Gibco Laboratories, USA) and 10 % fetal bovine serum (FBS, Gibco Laboratories, USA). The adenoviral vector used in this experiment was kindly supplied by Dr. Kuryk from the NIPH NIH - NRI in Poland. The vector underwent standard adenovirus preparation protocols for its generation and amplification, as previously described [27]. Briefly, three main modifications have been performed onto the Ad5 *wt* virus who served as backbone structure: (i) a 24-base pair deletion in the E1A conserved region; (ii) the insertion of the inducible costimulatory ligands ICOSL and CD40L under an exogenous promoter in the E3 region, (iii) Ad5/3 chimeric construct by alterations to the fiber knob. The Ad5/3-D24-ICOSL-CD40L and Ad5/3-D24-mCherry-ICOSL-CD40L (consisting of a 24-bp deletion in E1A Conserved Region 2 (CR2), a ICOSL-CD40L / mCherry-ICOSL-CD40L expression cassette inserted in the E3 region, and Ad5/3 hybrid fiber) have been produced, characterized and tested as described earlier [28,29]. ILDTAGREEY ($Q61R_{55–64}$), ILDTAGKEEY ($Q61K_{55–64}$), GLAPPQHLI ($P53_{187–195}$), SVYDFFVWL (TRP-$2_{180-188}$) were purchased from GeneCust (France). The net charge of the peptides was calculated using the Peptide Calculator software (Innovagen, Sweden).

2.2. Physico-chemical characterization by dynamic light scattering (DLS): zeta potential and size analysis

Investigated formulations used in this work were prepared by adding tested oncolytic adenoviruses to clinically relevant and previously published melanoma specific epitopes [30,31] (Table 1). The concentration of oncolytic adenovirus remained constant, while the amount of epitopes was incrementally increased, following the outlined procedure: (i) for each microliter of viral preparation employed (at a concentration of 10^9 VP/mL), the corresponding amount of peptide was determined

Table 1
Overview of the selected melanoma cell lines and the chosen epitopes.

Cell lines	Species	Mutation	Sequence	Allele (MHC class I)	Epitope origin
MUG Mel-2 A375	Human (melanoma)	NRAS Q61R	ILDTAGREEY	A*02:03	$Q61R_{55–64}$
	Human (melanoma)	NRAS Q61K	ILDTAGKEEY	A*01:01	$Q61K_{55–64}$
		B-RAF V600E	GLAPPQHLI	A*02:01	$P53_{187–195}$
B16V	Mouse (melanoma, C57BL/6)	Wild-type	SVYDFFVWL	H-2-Kb (mouse)	TRP-$2_{180-188}$

based on the desired concentration (0.1, 0.5, 1.5, 5, 10, 20, 40 μg/mL), (ii) the different formulations were then diluted, either in sterile Milli-Q water adjusted to pH 7.4, to a final volume of 700 μl for Zeta potential analysis. To determine the size, the different formulations were diluted in the appropriate cell culture medium supplemented with 10 % FBS (Gibco Laboratories, CA, USA), to a final volume of 100 μl, then each resulting sample was transferred to a polystyrene disposable cuvette to determine the size of the formulations. Subsequently, the sample was transferred to a DTS1070 disposable capillary cell (Malvern, Worcestershire, UK) for zeta potential measurements. All measurements were conducted at 25 °C using a Zetasizer Nano ZS instrument (Malvern).

2.3. Transmission-electron microscopy characterization

The morphology and structural characteristics of oncolytic adenovirus alone, and of the oncolytic vaccine were examined by transmission electron microscopy (TEM) with the Tecnai G2 microscope (FEI). Sample preparation followed the protocol outlined in the previous paragraph entitled "Zeta potential and dynamic light scattering (DLS) analysis", involving deposition onto a 400-mesh support grid coated with holey carbon, allowing solvent evaporation at room temperature. Subsequently, negative staining was performed using a 1 % *w/v* aqueous uranyl acetate solution prior to image acquisition. TEM images were obtained by rotating the sample over a range from +60° to −60°, with images taken at 2° intervals during rotation.

2.4. CAR and DSG2 expression in melanoma cell lines.

MUG Mel-2, A375 and B16V cells were seeded at the concentration of 5×10^5 cell/well in a 96 well plate with flat bottom and maintained under the above-described standard cell culture growth conditions. On the next day, cells were stained firstly with mouse monoclonal anti-CAR antibody (SantaCruz Biotech, Dallas, TX, USA) and then with 1:2000 Alexa-Fluor 488 secondary antibody (Abcam, Cambridge, UK) or mouse monoclonal anti-DSG2 antibody (Abcam, Cambridge, UK) and then with 1:2000 Alexa-Fluor 488 secondary (Beckman-Coulter Cytomics FC500). After 30 min incubation, samples were subjected to flow cytometric analysis using the BD FACSAria™ III instrument (New Jersey, USA).

2.5. Cell viability: MTS cytotoxicity assay.

MUG Mel-2 and A375 were seeded at a rate of 1×10^4 cells/well while B16V cells at a rate of 7×10^3 cells/well in a 96 well plate with a flat bottom and maintained under the above cell culture growth conditions. After overnight incubation, cells were treated according to conditions outlined in Table 2.

After 72 h post treatment cell viability was determined by using CellTiter 96 AQueous One Solution Cell Proliferation Assay (MTS) according to the manufacturer's instructions (Promega, Madison, WI, USA). The absorbance was measured with a 96-well plate spectrophotometer (Victor Nivo™, PerkinElmer, Milano, Italy) at 490 nm. The experiments were independently performed three times and each treatment was performed in triplicate.

Table 2
Treatment schedule for the assessment of tested anti-cancer agents *in vitro*.

Treatment conditions	Day 1 (24 h after seeding)	Day 2 (48 h after seeding)
Melanoma epitope ($Q61R_{55–64}$, $Q61K_{55–64}$, $P53_{187–195}$, $TRP\text{-}2_{180-188}$)	10 μg/mL	Treatment removal
Ad5/3-D24-ICOSL-CD40L	100 VP/cell	
Ad5/3-D24-ICOSL-CD40L + Melanoma epitope	100 VP/cell +10 μg/mL (epitope)	

2.6. Immunogenicity of tumor cell death in vitro

ATP release: melanoma cells were seeded at 1×10^4 cells/well and 7×10^3 cells/well, respectively, in a 96-well plate with flat bottom. On the following day, cells were treated as outlined in Table 2. After 72 h of incubation, cells have been analyzed with an ATP detection kit (CellTiter-Glo® Luminescent Cell Viability Assay, Promega) according to the manufacturer's protocol for luminometric analysis (Victor Nivo™). The experiments were independently performed three times and each treatment was performed in replicates.

Calreticulin (CRT) exposure: human and murine melanoma cell lines were seeded onto 24-well plates at a density of 5×10^4 cells/well and maintained under standard growth conditions. On the following day, cells were subjected to the treatments as described in Table 2. Then, 48 h after treatment, cells were harvested and stained with 1:1000 diluted Alexa-Fluor 488 rabbit polyclonal anti-calreticulin antibody (Abcam, Cambridge, UK) (concentration of 1 μg/mL) or Alexa Fluor Plus 488 goat anti-mouse at the concentration 1–10 μg/mL (ThermoFisher, Scientific, A32723, Waltham, MA, USA) for 30 min and analyzed by flow cytometry analysis using BD FACSAria™ III instrument (New Jersey, USA). The experiments were independently conducted three times, with three replicates for each treatment.

2.7. Confocal microscopy studies

Cells were seeded on 24-chamber glass slides (Sigma-Aldrich, St. Louis, MO, USA) in a 24 well plate at a concentration of 10^5 cells/well for MUG Mel-2 and A375 while B16V were seeded at a concentration of 7×10^4 cells/well in the appropriated cell culture medium.

After overnight incubation, cells were treated according to the conditions detailed in Table 2. Herein, Ad5/3-D24-mCherry-ICOSL-CD40L and melanoma epitopes, labeled with FITC were used. After incubation at the chosen time points (4, 8, 24, 48, 72 h), cells were washed three times with PBS and fixed with 4 % *w/v* paraformaldehyde in PBS for 15 min. Nuclei were stained with DAPI (Thermo Scientific) and incubated for 10 min at 37°. Between these steps, cells were washed three times with PBS. Cover glasses have been removed from plates and mounted in microscope slides (Menzel-Glaser) with Prolong™ Glass Antifade mountant (Invitrogen). Confocal analysis was performed by using Zeiss LSM800 equipped with 63× oil objective. Lasers at 385/30 nm, 495/519 nm and 631/33 nm were used to detect fluorescence of DAPI, FITC and mCherry, respectively. Image analyses were performed using ImageJ (NIH, USA).

2.8. 3D-cell culture establishment

For spheroids formation, MUG Mel-2 cells were seeded at a density rate of 1×10^4 cells/well in 96-well plates with flat bottom, previously coated with 50 μl of 1.5 % agarose solution (Thermo Scientific, Waltham, Massachusetts, USA). After seeding, the plates were centrifuged at 1000 rpm for 5 min. After 4 days from spheroids formation, treatments were performed as reported in Table 3. Every three days spheroids areas were registered using imaging software (AxioVision software by Zeiss, Oberkochen, Germany). The volume of the 3D tumor spheroids was calculated based on measurements of their orthogonal diameters using the formula $0.52 \times \text{length} \times (\text{width})^2$.

2.9. Establishment of 3D Co-cultures of MUG Mel-2 cells and peripheral blood mononuclear cells (PBMCs)

Prior to the experiment, PBMCs were purchased from Stemcell Technologies (Vancouver, British Columbia, Canada) and stored in liquid nitrogen until they were used in co-culture with the cancer cells. MUG Mel-2 cells were stained, according to the manufacturer's instructions, with carboxyfluorescein succinimidyl ester (CFSE, Sigma-Aldrich, Saint Louis, MO, USA) while the CellTracker Orange CMTMR

Table 3
Treatment schedule for 3D cell culture melanoma model.

Conditions/ Days	Day 0	Day 7	Day 10	Day 13	Day 16	Endpoint
Control	MUG Mel-2 cells seeded on a 96 well plate previously coated with 1.5 % agarose at a rate of 1 × 10^4 cells/ well	Medium change				Follow up until day 31 Medium change once a week Size and dimensions registered every 3 days
$Q61R_{55–64}$		10 μg/ mL	10 μg/ mL	10 μg/ mL	Medium change	
Ad5/3-D24-ICOSL-CD40L		10^9 VP/ ml	10^9 VP/ ml	10^9 VP/ ml	Medium change	
Ad5/3-D24-ICOSL-CD40L + $Q61R_{55–64}$		10^9 VP/ ml + 10 μg/ mL	10^9 VP/ ml + 10 μg/ mL	10^9 VP/ ml + 10 μg/ mL	Medium change	

(C2927, Invitrogen, Waltham, Massachusetts, USA) was used to stain PBMCs following the manufacturer's instructions. MUG Mel-2 cell lines, previously stained with cell trace CFSE, were seeded at a density of 7500 cells/well in 96-well plates with flat bottom, previously coated with 50 μL of an 1.5 % agarose solution (Thermo Scientific, Waltham, Massachusetts, USA). After seeding, the plates were centrifuged at 1000 rpm for 5 min, to allow spheroids formation. At day 6, co-culture can be assembled and PBMCs, already stained with CellTracker Orange, were added to the spheroids in a ratio 1:4. After 24 h, images were acquired using a 10× fluorescence microscope objective (Nikon Ts).

2.10. 3D Co-culture treatment

MUG Mel-2 cells were seeded on a 96-well plate previously coated with 50 μl of an 1.5 % agarose solution at a density of 7500 cells/well. On day 6, after spheroids formation, the infiltration of PBMCs into tumor cell-spheroids was performed as previously described [27] in a 1:4 ratio. At day 7, cells were treated according as detailed in Table 4. Specifically, the spheroids received the following treatments: (i) culture media, (ii) $Q61R_{55–64}$ (10 μg/mL), (iii) Ad5/3-D24-ICOSL-CD40L (10^9 VP/mL), (iv) Ad5/3-D24-ICOSL-CD40L (10^9 VP/mL) + $Q61R_{55–64}$ (10 μg/mL). Treatments were administered every three days and culture medium was changed once a week. Spheroid's size was measured on two dimensions every three days while the volume was obtained by applying the formula 0.52 × length×$(width)^2$. The area was measured using AxioVision software by Zeiss.

Table 4
Treatment schedule for the 3D co-culture melanoma model.

Conditions/ Days	Day 0	Day 7	Day 10	Day 13	Day 16	Endpoint
Control	MUG Mel-2 cells seeded on a 96 well plate previously coated with 1.5 % agarose at a rate of 1 × 10^4 cells/ well	Medium change				Follow up until day 31 Medium change once a week Size and dimensions registered every 3 days
$Q61R_{55–64}$		10 μg/ mL	10 μg/ mL	10 μg/ mL	Medium change	
Ad5/3-D24-ICOSL-CD40L		10^9 VP/ ml	10^9 VP/ ml	10^9 VP/ ml	Medium change	
Ad5/3-D24-ICOSL-CD40L + $Q61R_{55–64}$		10^9 VP/ ml + 10 μg/ mL	10^9 VP/ ml + 10 μg/ mL	10^9 VP/ ml + 10 μg/ mL	Medium change	

2.11. Immune cell infiltrates – in vitro analysis

The percentage number of human immune cell populations were monitored by flow cytometry: hCD45+ lymphocytes (BD, cat. Number: 564105), T cells hCD3+ (BD, cat. Number: 555339), CD4+ T cells (hCD3+ hCD4+, BD, cat. Number: 557852), CD8+ T cells (hCD3+ hCD8+, BD, cat. Number: 560179). Tumors (spheroids) were harvested and subsequently dissociated with cell strainer (Day 31 – end of study). After dissociation, cells were washed using BD Perm/Wash™ buffer (cat. no. 554723) and stained with antibodies for 30 min at 4 °C in the dark and then suspended in stain buffer FBS (BD, cat no. 554656). Samples were acquired using BD Lyric FACS Flow. The populations were gated with forward and side scattering (FSC-A/SSC-A dot plot) in leukocytic regions, as described previously [29]. Flow cytometry analysis was performed on FlowJo v10 software.

2.12. Production of EVs and peptide loaded EVs

In order to produce EVs, 8 × 10^6 MUG Mel-2 cells were plated into T-175 flask in medium supplemented with 5 % FBS. The FBS growth media was ultra-centrifuged overnight (110,000 x*g* at 4 °C for 18 h, Optima MAX-XP ultracentrifuge, rotor MLA-80, Beckman Coulter) to remove EVs present in the serum. EVs were isolated from the conditioned medium using differential centrifugation steps. First the conditioned medium was centrifuged at 500 x*g* in 4 °C for 10 min to pellet cells (Centrisart G-16C Centrifuge, Sartorius). Then, the supernatant was collected and ultracentrifuged for 2 h at 100000 x g in 4 °C, using XL-70 ultracentrifuge (Beckman Coulter) with rotor 50Ti (Beckman Coulter). The supernatant was aspirated and EV- containing pellets re-suspended in PBS (Aurogene, Rome, Italy) 100 μL and stored at −80 °C.

EVs were loaded with melanoma epitope $Q61R_{55–64}$ and prepared by incubating 1 × 10^8–5 × 10^9 EVs with 10 μg/mL $Q61R_{55–64}$ (Genecust, France) per mL of EV suspension in PBS for 1 h at RT. Next, the samples were centrifuged at 150000 ×*g* for 3 h to pellet the EVs. The supernatant containing unbound epitope was removed, and the EV-pellet was washed by suspending it in PBS and pelleting it again at 150000 ×*g*.

2.13. Production of EV-Virus, oncolytic vaccine loaded EVs and indocyanine green loaded EVs

EV-encapsulated virus (EV-Virus) were produced as previously described [22,23] 8 × 10^6 of MUG Mel-2 cells were infected with 10 viral particles/cell of Ad5/3-D24-ICOSL-CD40L and were cultured at 37 °C and 5 % CO2. 48 h later when most of the cells were detached from the culture flask, the culture media were collected for EV-Virus isolation using differential centrifugation. First the conditioned medium was centrifuged at 500 ×*g* and 4 °C for 10 min, to separate the cells (Centrisart G-16C Centrifuge, Sartorius). Then, the supernatant containing EV-Virus was collected and ultra-centrifuged for 2 h at 100000 ×*g* and 4 °C, using XL-70 ultra-centrifuge (Beckman Coulter) with rotor 50Ti (Beckman Coulter). The supernatant was aspirated and pellets containing EV-Virus re-suspended in PBS 100 μL and stored at −80 °C. EV-Virus samples were incubated in 100 mM NaOH at room temperature for 20 min to inactivate any free not EV encapsulated virus present as previously reported [22,24].

To generate oncolytic vaccine loaded EVs (EV-Virus-$Q61R_{55–64}$), 1 × 10^8–5 × 10^9 EV-Virus was incubated for 1 h at RT with 10 μg/mL $Q61R_{55–64}$ (per mL of EV-Virus suspension) in PBS. Next, the samples were centrifuged at 150000 ×*g* for 3 h to pellet the EV-Virus-$Q61R_{55–64}$. The supernatant containing unbound epitope was removed, and the EV-Virus-$Q61R_{55–64}$ pellet was washed by suspending it in PBS and pelleting it again at 150000 ×*g*.

To label EVs and EV-virus formulations, EVs were loaded with ICG by incubating 1 × 10^8–5 × 10^9 EVs in PBS for 12 h at 4 °C with 50 μg/mL ICG (Sigma). Next, the samples were centrifuged at 150000 ×*g* for 3 h to pellet the EVs. The supernatants containing unbound ICG were removed,

and the pellet was washed by suspending it in PBS and pelleting it again at 150000 ×*g*. In order to load FITC-Q61R$_{55–64}$ within labeled EV-ICG-virus formulations, the melanoma epitope was left to incubate in PBS for 1 h at 4°. Next, the samples were centrifuged at 150000 ×*g* for 3 h to pellet the EV-ICG-Ad5/3-D24-mCherry-ICOSL-CD40L-FITC-Q61R$_{55–64}$ formulations and then, resuspended in PBS.

2.14. Size distribution analysis by nanoparticle tracking analysis (NTA)

Size distribution and concentration of EV, EV-Virus, EV-Virus-Q61R$_{55–64}$, EV-Q61R$_{55–64}$ formulations were analyzed by NTA using Nanosight model LM14 (Nanosight) equipped with blue (404 nm, 70 mV) laser and sCMOS camera. The samples containing virus were incubated at +95 °C for 10 min to inactivate the viruses. NTA was performed for each sample by recording three 90 s videos, subsequently analyzed using NTA software 3.0 (Nanosight). The detection threshold was set to level 5 and camera level to 15.

2.15. Cryo-EM

Cryo-EM images were acquired with a FEI Talos Arctica 200 kV FEG electron microscope equipped with a FEI Falcon 3EC direct electron detector and Volta Phase-plate. Prior to Cryo-EV imaging, samples were vitrified on a FEI Vitrobot IV apparatus and then processed.

2.16. Western blot analysis

Ultracentrifuged EVs pellets were re-suspended in home-made lysis buffer 30 μL (Bio-Rad recipe) for western blot assay. Proteins were quantified thanks to bicinchoninic acid assay (EuroClone, EMP014500), and a total amount of 20 μg of proteins were separated on a 4–20 % Mini-PROTEAN® TGX™ Precast Protein Gels (Bio-Rad, cat. 4,561,094) under reducing conditions for 1 h at 110 V on Mini-PROTEAN Tetra Vertical Electrophoresis Cell by Bio-Rad (cat. 1,658,004). Proteins were then transferred onto a 0.2 μm nitrocellulose membrane (Bio-Rad, cat. 1,704,158) by the means of a semi-dry Trans-Blot® Turbo™ Transfer System (Bio-Rad, cat. 1,704,150). Membranes were blocked with 5 % *w/v* of non-fat dry milk in TBS-Tween 20 1× (blocking solution) for 1 h at room temperature in agitation and then incubated with primary antibodies solutions overnight at 4 °C in agitation. Primary antibodies were diluted in blocking solution according to manufacturers' instructions: GAPDH 1:5000 (GeneTex, cat. GTX100118), Calnexin 1:5000 (GeneTex, cat. GTX112886), CD29 1:5000 (GeneTex, cat. GTX128839) TSG101 1:500 (GeneTex, cat. GTX70255), CD81 1:200 (GTX101766), CD9 1:1000 (Abcam, cat. ab236630). The day after, the membranes were washed with TBST20 1× three times, 15 min each, and then incubated at room temperature for 1 h 30 min with secondary antibodies solutions, in agitations. Secondary antibodies were diluted in blocking solution according to manufacturers' instructions: goat anti-rabbit 1:5000 (Jackson ImmunoResearch, cat. 111–036-045), goat anti-mouse 1:5000 (Jackson ImmunoResearch, cat. 115–036-062). Upon three washes as before, specific immunobands were detected with Alliance Q9 detection system (Uvitec) after 5 min incubation in the dark with ECL solution (EuroClone, cat. EMP001005).

2.17. Confocal microscopy studies on EV loaded formulations

MUG Mel-2 cells were seeded on 24-chamber glass slides (Sigma-Aldrich, St. Louis, MO, USA) in a 24 well plate at a concentration of 10^5 cells/well in the appropriated cell culture medium. After overnight incubation, cells were treated with EV-ICG formulations loaded with FITC-Q61R$_{55–64}$ and Ad5/3-D24-mCherry-ICOSL-CD40L. After 24 h cells were washed three times with PBS and fixed with 4 % *w/v* paraformaldehyde in PBS for 15 min. Nuclei were stained with DAPI (Thermo Scientific) and incubated for 10 min at 37°. Between these steps, cells were washed three times with PBS. Cover glasses have been removed from plates and mounted in microscope slides (Menzel-Glaser) with Prolong™ Glass Antifade mountant (Invitrogen). Confocal analysis was performed by using Zeiss LSM800 equipped with 63× oil objective. Lasers at 385/30 nm, 495/519 nm, 631/33 nm and 789/814 nm were used to detect fluorescence of DAPI, FITC, mCherry and ICG, respectively. Image analyses were performed using ImageJ (NIH, USA).

2.18. In vivo studies

Animal procedures were approved by the Italian Ministry of Health and the Warsaw University of Life Sciences' II Local Ethical Committee for Animal Experiments. For the *in vivo* studies, melanoma human xenografts were established by injecting 2 × 10^6 MUG Mel-2 cells subcutaneously (s.c.) into both flanks of BALB/c nude mice and in the neck of human CD34$^+$ hematopoietic stem- cell-engrafted NSG variant mice (8 tumors per group). Prior to the start of treatment, tumors of sizes ~5 × 5 mm in diameter were randomized. Mice were given treatments intratumorally (i.t) according to the ones enlisted in Tables 5, 6 and 7 (immunodeficient melanoma MUG Mel-2 mouse model and humanized MUG Mel-2 mouse model). At least twice a week, the size of the tumor was measured using a caliper in two dimensions. At each timepoint, the longest and shortest diameters of the tumor were measured, and the tumor volume was computed using the formula 0.52 length × (width)^2. Tolerability of the treatments was assessed by measuring the body weight once a week. All animals were observed for clinical signs, morbidity, or mortality daily during the acclimatization and administration period and additionally 30 min after each treatment.

2.19. In vivo and ex vivo fluorescence imaging

In vivo and *ex vivo* fluorescence imaging was carried out 24 h post i.v. EV treatments, mice were anaesthetized using Isoflurane (Isoflurane-Vet; Merial, Lyon, France) and kept under anesthesia during imaging sessions carried out using a IVIS camera (PerkinElmer), equipped with suitable filters (ICG, mCherry, FITC) following the manufacturer's instructions. Mice were anaesthetized using isoflurane (Isoflurane-Vet; Merial, Lyon, France) and kept under anesthesia during imaging sessions. For *ex vivo* imaging, mice were sacrificed by cervical dislocation and *ex vivo* imaging of the fluorescence signal from selected organs was carried out.

2.20. Immune cell infiltration analysis- ex vivo analysis

The percentage number of human immune cell populations were monitored by flow cytometry: hCD45$^+$ lymphocytes (BD, cat. Number: 564105), T cells hCD3$^+$ (BD, cat. Number: 555339), CD4$^+$ T cells (hCD3$^+$ hCD4$^+$, BD, cat. Number: 557852), CD8$^+$ T cells (hCD3$^+$ hCD8$^+$, BD, cat. Number: 560179). Tumors (spheroids) were harvested and subsequently dissociated with cell strainer (Day 31 – end of study). After dissociation, cells were washed using BD Perm/Wash™ buffer (cat. no. 554723) and stained with antibodies for 30 min at 4 °C in the dark and then suspended in stain buffer FBS (BD, cat no. 554656). Samples

Table 5
Treatment schedule for *in vivo* efficacy studies in immunodeficient xenograft MUG Mel-2 melanoma model.

Group	Day 0	Day 3	Day 6	Day 9	Day 12	Day 15
1. Control	PBS	PBS	PBS	PBS	PBS	PBS
2. Q61R-$_{55-64}$	10 μg/mL i.t.	10 μg/mL i.t.	10 μg/mL i.t.	10 μg/mL i.t.	10 μg/mL i.t.	10 μg/mL i.t.
3. Ad5/3-D24-ICOSL-CD40L	10^9 VP i.t.	10^9 VP i.t.	10^9 VP i.t.	10^9 VP i.t.	10^9 VP i.t.	10^9 VP i.t.
4. Ad5/3-D24-ICOSL-CD40L + Q61R-$_{55-64}$	10^9 VP + 10 μg/mL i.t.	10^9 VP + 10 μg/mL i.t.	10^9 VP + 10 μg/mL i.t.	10^9 VP + 10 μg/mL i.t.	10^9 VP + 10 μg/mL i.t.	10^9 VP + 10 μg/mL i.t.

Table 6
Treatment schedule for biodistribution study in humanized MUG Mel-2 melanoma model.

Group	Day 0	Day 3	Day 6	Day 9	Day 12	Day 15
1. EV-ICG	1×10^9 particles i.v.	1×10^9 particles i.v.	1×10^9 particles i.v.	1×10^9 particles i.v.	1×10^9 particles i.v.	1×10^9 particles i.v.
2. Virus-mCherry	1×10^8 VP i.v.	1×10^8 VP i.v.	1×10^8 VP i.v.	1×10^8 VP i.v.	1×10^8 VP i.v.	1×10^8 VP i.v.
3. EV-ICG-Virus-mCherry	1×10^9 particles; 1×10^8 VP and 50 μg/mL of ICG i.v.	1×10^9 particles; 1×10^8 VP and 50 μg/mL of ICG i.v.	1×10^9 particles; 1×10^8 VP and 50 μg/mL of ICG i.v.	1×10^9 particles; 1×10^8 VP and 50 μg/mL of ICG i.v.	1×10^9 particles; 1×10^8 VP and 50 μg/mL of ICG i.v.	1×10^9 particles; 1×10^8 VP and 50 μg/mL of ICG i.v.
4. 3. EV-ICG-Virus-mCherry-FITC-Q61R$_{55–64}$	1×10^9 particles, 1×10^8 VP, 10 μg/ml, 50 μg/mL of ICG i.v.	1×10^9 particles, 1×10^8 VP, 10 μg/ml, 50 μg/mL of ICG i.v.	1×10^9 particles, 1×10^8 VP, 10 μg/ml, 50 μg/mL of ICG i.v.	1×10^9 particles, 1×10^8 VP, 10 μg/ml, 50 μg/mL of ICG i.v.	1×10^9 particles, 1×10^8 VP, 10 μg/ml, 50 μg/mL of ICG i.v.	1×10^9 particles, 1×10^8 VP, 10 μg/ml, 50 μg/mL of ICG i.v.
5. FITC-Q61R$_{55–64}$	10 μg/ml i.v.	10 μg/ml i.v.	10 μg/ml i.v.	10 μg/ml i.v.	10 μg/ml i.v.	10 μg/ml i.v.
6. ICG	50 μg/mL of ICG i.v.	50 μg/mL of ICG i.v.	50 μg/mL of ICG i.v.	50 μg/mL of ICG i.v.	50 μg/mL of ICG i.v.	50 μg/mL of ICG i.v.

Table 7
Treatment schedule for *in vivo* efficacy study in humanized MUG Mel-2 melanoma model.

Group	Day 0	Day 3	Day 6	Day 9	Day 12	Day 15
1. EV	1×10^9 particles i.v.	1×10^9 particles i.v.	1×10^9 particles i.v.	1×10^9 particles i.v.	1×10^9 particles i.v.	1×10^9 particles i.v.
2. EV-Q61R$_{55–64}$	1×10^9 particles +10 μg/ml i.v.	1×10^9 particles +10 μg/ml i.v.	1×10^9 particles +10 μg/ml i.v.	1×10^9 particles +10 μg/ml i.v.	1×10^9 particles +10 μg/ml i.v.	1×10^9 particles +10 μg/ml i.v.
3. Q61R$_{55–64}$	10 μg/ml i.v.	10 μg/ml i.v.	10 μg/ml i.v.	10 μg/ml i.v.	10 μg/ml i.v.	10 μg/ml i.v.
4. Virus + Q61R$_{55–64}$	1×10^8 VP, 10 μg/ml i.v.	1×10^8 VP, 10 μg/ml i.v.	1×10^8 VP, 10 μg/ml i.v.	1×10^8 VP, 10 μg/ml i.v.	1×10^8 VP, 10 μg/ml i.v.	1×10^8 VP, 10 μg/ml i.v.
5. EV-Virus	1×10^9 particles; 1×10^8 VP i.v.	1×10^9 particles; 1×10^8 VP i.v.	1×10^9 particles; 1×10^8 VP i.v.	1×10^9 particles; 1×10^8 VP i.v.	1×10^9 particles; 1×10^8 VP i.v.	1×10^9 particles; 1×10^8 VP i.v.
6. EV-Virus-Q61R$_{55–64}$	1×10^9 particles, 1×10^8 VP, 10 μg/ml i.v.	1×10^9 particles, 1×10^8 VP, 10 μg/ml i.v.	1×10^9 particles, 1×10^8 VP, 10 μg/ml i.v.	1×10^9 particles, 1×10^8 VP, 10 μg/ml i.v.	1×10^9 particles, 1×10^8 VP, 10 μg/ml i.v.	1×10^9 particles, 1×10^8 VP, 10 μg/ml i.v.

were acquired using BD Lyric FACS Flow. The populations were gated with forward and side scattering (FSC-A/SSC-A dot plot) in leukocytic regions, as described previously [29]. Flow cytometry analysis was performed on FlowJo v10 software.

2.21. Confocal imaging of explanted specimens

Tissues from tumor and liver underwent routine paraffin processing followed by sectioning at 10 μm thick sections for fluorescence imaging. The slides were then analyzed using a confocal microscope (Zeiss LSM800) equipped with 40× oil objective to acquire the fluorescence signals released by ICG, mCherry and FITC. Throughout the process of fixation and paraffin-embedding, the samples were kept in the dark to avoid loss of the fluorescence signal. Lasers at 385/30 nm, 495/519 nm, 631/33 nm and 789/814 nm were used to detect fluorescence of DAPI, FITC, mCherry and ICG, respectively. Image analyses were performed using ImageJ (NIH, USA).

2.22. Statistical analysis

Data were reported as mean ± SEM or as indicated. Statistical analysis was performed with GraphPad Prism software version 9 (La Jolla, San Diego, CA, USA). An un-paired test and one-way ANOVA with the Krusal–Wallis test was used to compare two or more groups.

3. Results and discussion

3.1. Physico-chemical characterization of the oncolytic vaccine

Several studies have shown that melanoma is an immunogenic malignancy thus being a natural target to test novel immunotherapies [32]. While targeted immunotherapies have significantly enhanced the overall survival of non-NRAS mutated melanoma patients [33], those with NRAS mutations experience a comparatively poorer prognosis which can be attributed to a immunosuppressive tumor microenvironment [34], the absence of effective targeted therapies [35], and the emerging resistance to current treatments [36]. Peptide-based vaccines are used to direct the immune-response to a specific target, nevertheless when given alone as vaccines do not elicit strong immune responses due to their quick degradation at the injection site thus many patients do not benefit from them due to lack of optimal immune responses [37]. Given their direct lytic and immune-stimulating properties, OVs are particularly attractive for promoting long-lasting anti-cancer immune responses and clinical efficacy [38,39]. Previously we have shown that Ad5/3-D24-ICOSL-CD40L, able to encode for two co-stimulatory molecules ICOSL and CD40L [26] can modulate anti-cancer immune responses thus converting tumor immunosuppression to immunomodulation and improving melanoma treatment efficacy. Herein, in the current study, we aimed to administer the oncolytic adenovirus Ad5/3-D24-ICOSL-CD40L with MHC-I chosen NRAS mutated melanoma epitopes, where the adenoviral vector acts as natural immune activator.

We first investigated the surface charge properties of the combinatorial approach. The adenovirus capsid is recognized for its predominantly negatively charged nature, primarily attributable to the acidic regions within the hexon protein [40]. The combination with selected melanoma epitopes, specifically ILDTAGREEY (Q61R$_{55–64}$), ILDTAGKEEY (Q61K$_{55–64}$), GLAPPQHLI (P53$_{187–195}$), SVYDFFVWL (TRP-2$_{180-188}$), has been shown to influence the charge characteristics of the formulation depending on the amino acidic nature of the epitopes (Supplementary Fig. 1E). Formulations comprising Ad5/3-D24-ICOSL-CD40L, in conjunction with increasing concentrations of peptides (0.1, 0.5, 1.5, 5, 10, 20, 40 μg/mL), underwent comprehensive analysis of surface charge utilizing dynamic light scattering (DLS). Obtained data revealed an average *Z*-potential of approximately −20 mV (Supplementary Fig. 1A-D), consistent with the inherent negative charge of Ad5/3-D24-ICOSL-CD40L. Notably, epitopes ILDTAGREEY (Q61R$_{55–64}$), ILDTAGKEEY (Q61K$_{55–64}$) and GLAPPQHLI (P53$_{187–195}$), containing positively charged amino acids (R for arginine, K for lysine, and H for histidine, respectively), exhibited an increase in Z-potential up to an approximate plateau of 0 mV (Supplementary Fig. 1A-D). Conversely, SVYDFFVWL (TRP-2$_{180-188}$) lacked positively charged amino acids in its sequence, leading to a continuous decrease in terms of Z-potential due to the increase of negative charges on the surface of the adenoviral capsid.

These findings elucidate the dynamic interplay between epitope sequences and the charge characteristics of the adenovirus capsid.

To further investigate the stability of tested agents, size was measured by dynamic light scattering analysis. Adenovirus size alone was measured to assess the difference in the presence of serum proteins and in milliQ water. By comparing increasing viral particles (1×10^8–1×10^{11} VP/mL), no significant changes have been detected (Supplementary Fig. 2A), as confirmed by TEM imaging (Supplementary Fig. 2F), where an average of 97.75 nm in terms of size was shown. Combinations of Ad5/3-D24-ICOSL-CD40L and melanoma epitopes (ILDTAGREEY (Q61R$_{55–64}$), ILDTAGKEEY (Q61K$_{55–64}$), GLAPPQHLI (P53$_{187–195}$) and SVYDFFVWL (TRP-2$_{180-188}$)) shows that the oncolytic vaccine maintained its stability except for the highest peptide quantity where the equilibrium is slightly destabilized, resulting in a bulkier system by exceeding 10 μg/mL peptide concentration, that represent the plateau reached by the combinatorial approach. Therefore, melanoma epitopes to be used for further *in vitro* and *in vivo* investigations were selected as a common choice at 10 μg/mL (Supplementary Fig. 2F) since it represents the best concentration by which we can exploit its role in eliciting an immunomodulatory action preventing a cost-effective and resource-intensive consequence, and can lead to unwanted effects, such as toxicity and adverse reactions [41,42].

3.2. Evaluation of cell cytotoxicity and transduction efficiency in 2D melanoma culture models

The first step in assessing the possibility of using Ad5/3-D24-ICOSL-CD40L against melanoma is to determine the expression of adenoviral receptors which are needed for the viral internalization on a panel of different melanoma cell lines (B16V, A375, MUG Mel-2). The rationale behind this investigation is that the relevant and continuous expression of these receptors allows higher internalization of viral particles and consequent increased noticeable infectivity [43].

All human melanoma cell lines expressed a notable level of DSG-2 receptors (MUG Mel-2: 93.04 % and A375: 99.95 %) (Supplementary Fig. 3B—C), compared to the murine B16V (21.2 %) (Supplementary Fig. 3 A). The expression of CAR receptors was lower but detectable, across all designated cell lines (B16V: 1.15 %; MUG Mel-2: 70.67 %; A375: 92.45 %), indicating that both receptors can be exploited by the adenoviral vector to facilitate its internalization in selected cell lines, thus the chimeric fiber knob can result in an enhancement of the infectivity. These findings align with previous research [43], which identified DSG-2 as the preferred target for the adenovirus internalization.

In this study, human A375 cell line was used as a model for NRAS (Q61K) and V-600E BRAF mutated melanomas. Therefore, we have tested Q61K$_{55–64}$ and P53$_{187–195}$ (negative control for NRAS) epitopes, respectively, combined with Ad5/3-D24-ICOSL-CD40L. Additionally, the human MUG Mel-2 (Q61R) cell line and murine B16V (TRP-2, negative control for NRAS) were used to investigate the role of the combinatorial approach in NRAS mutated melanomas and wild-type melanoma, respectively, by combination of the adenoviral vector with Q61R$_{55–64}$ and TRP-2$_{180-188}$. The *in vitro* efficacy of the novel Ad5/3-D24-ICOSL-CD40L alone and its combination with melanoma epitopes was tested to check whether the presence of the tumor peptides could affect the *in vitro* oncolytic activity. Our results show an enhanced reduction of cell viability in the virus and combination-treated cells in all the tested melanoma cell lines, compared to untreated control cells (Fig. 1 A-D). The combinatory therapy of both tested oncolytic adenoviruses with melanoma epitopes did not change the overall *in vitro* efficacy of the oncolytic vector. This is not surprising, as the model cannot assess the immunomodulatory properties of the cancer vaccine due to the absence of immune cells.

To further evaluate the effect of Ad5/3-D24-mCherry-ICOSL-CD40L and its combination with melanoma epitopes on selected melanoma cells, confocal microscopy analysis was performed by assessing the transfection through fluorescent protein visualization (Fig. 2). The progress of the viral infection and peptide internalization could be followed by detecting the emission signal of the protein fluorophore mCherry (excitation λ: 540–590 nm; emission λ: 550–650) expressed by the virus and FITC (excitation λ: 517 nm; emission λ: 498 nm) conjugated to the peptides. The more intense the emission of this signal, the greater the concentration of the fluorophore, and consequently, it correlates with the infecting virus presence inside tumor cells (Fig. 2).

This study allowed us to investigate morphological changes, induced by the different treatments, and at the same time to gain insights into the time required for the internalization of the vaccine, thus providing a comprehensive view of the uptake. The outcomes revealed a notable increase in fluorescence over time concerning both mCherry and FITC, a trend that was consistent across the different cell lines (Fig. 2A) thus suggesting their internalization into cells. Notably, throughout the study, morphological alterations and a general cytopathic effect in the treated cells were observed, especially for the human MUG Mel-2 cell line, a clear indication of the oncolytic efficacy already established. These results align with the ones obtained in the evaluation of the cell-killing activity, thus confirming the oncolytic activity of the vector in all the tested melanoma cell lines.

A comprehensive extension of the internalization investigation relies on the detailed co-localization analysis of the oncolytic vector and melanoma epitopes (Fig. 2B). As previously mentioned, this study aimed to shed light on the dynamic interplay between the oncolytic vaccine components, particularly focusing on the possible interaction between the virus and specific melanoma epitopes. The findings in the human melanoma cell lines (MUG Mel-2 and A375), provided a visually yellowish signal dominating the scene (Fig. 2B), indicative of the robust co-localization of the two vaccine components. In contrast, the murine B16V cell line produced a pronounced orange-ish signal, attributed to the completely negatively charged nature of TRP-2$_{180-188}$ neoantigen (Fig. 2B).

These changes and collective results, exhibiting enhanced

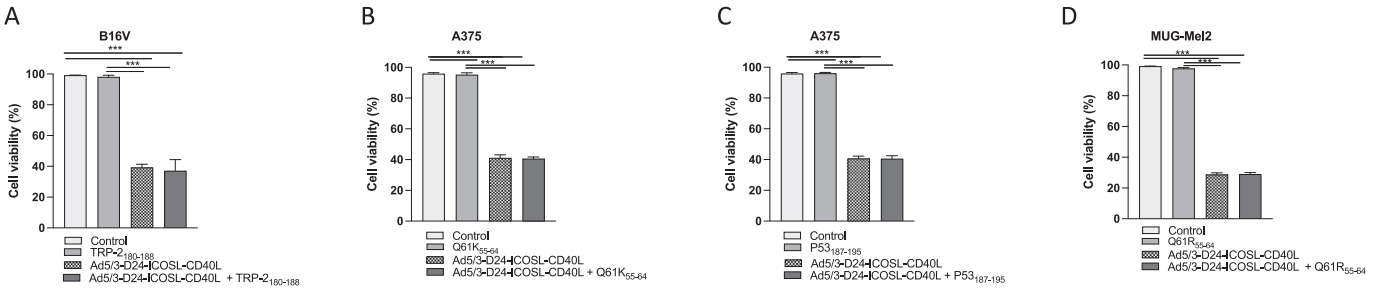

Fig. 1. Evaluation of cell viability by MTS assay. Cell viability was evaluated on MUG Mel-2, A375 and B16V cells 72 h post-treatments (Ad5/3-D24-ICOSL-CD40L at the concentration of 100 VP/cell, the selected tumor epitopes at the concentration of 10 μg/mL). Data are expressed as the percentage of viable cells, determined using CellTiter 96 Aqueous One Solution Cell Proliferation Assay (MTS) and measuring the absorbance at 490 nm with a 96-well plate spectrophotometer Viktor Nivo™. Statistical analysis was performed with *t*-test (***$P \leq 0.001$).

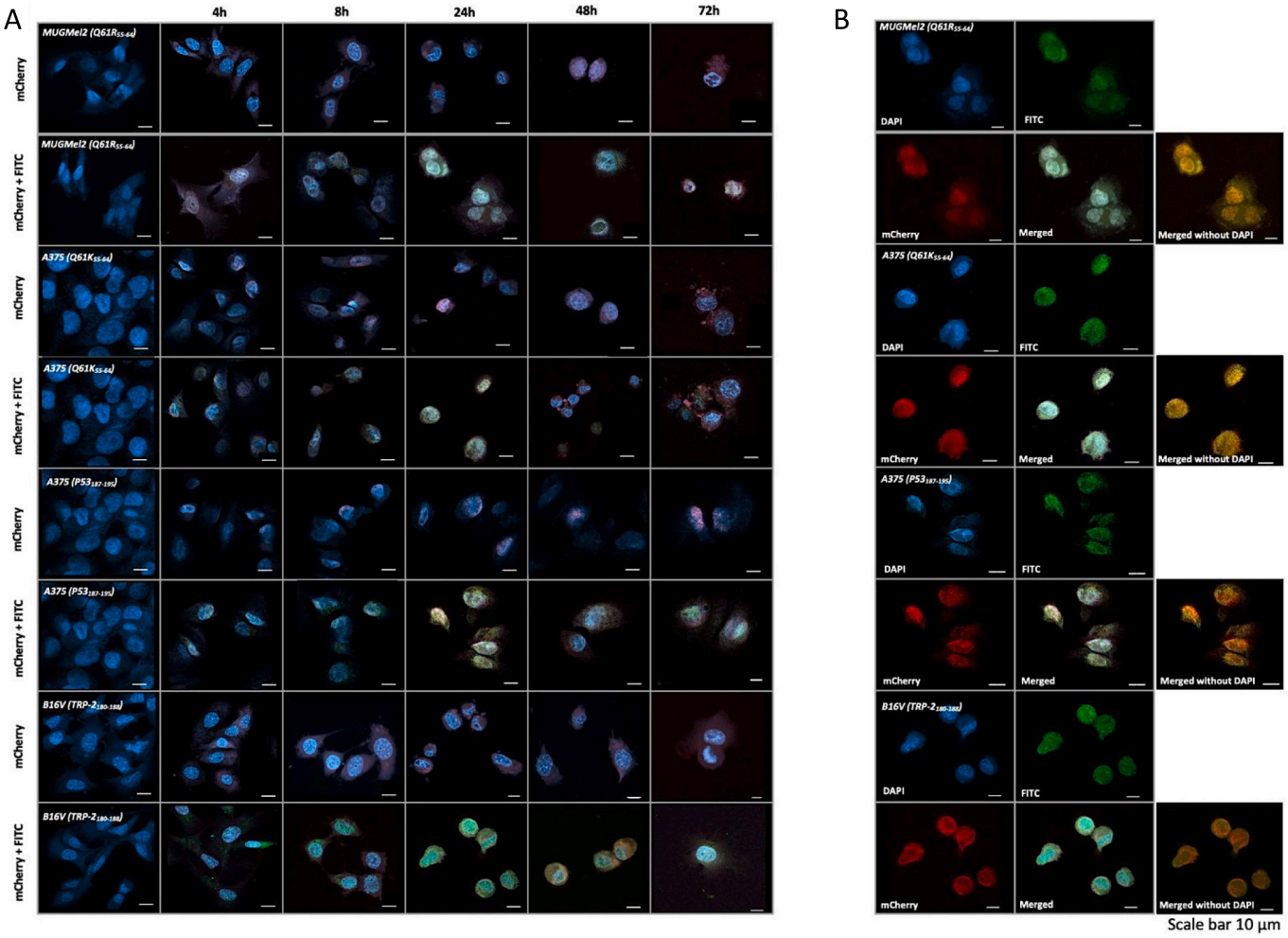

Fig. 2. Transduction efficiency assessed by confocal microscopy. (A) Melanoma cells MUG Mel-2, A375 and B16V were seeded on 24-chamber glass slides (Sigma–Aldrich, St. Louis, MO, USA) in a 24 well plate at a concentration of 10^5 cells/well. After treatment with Ad5/3-D24-mCherry-ICOSL-CD40L and the selected tumor epitopes, respectively at the concentration of 100 VP/cell and 10 µg/mL, cells were washed three times with PBS (Aurogene) and then fixed with 4 % (*w/v*) paraformaldehyde in PBS for 15 min. Nuclei were stained with DAPI (Thermo Scientific) incubated for 10 min. Confocal analysis was performed by Zeiss LSM800 equipped with 63× oil objective. Lasers at 385/30 nm, 495/519 nm and 631/33 nm were used to detect fluorescence of DAPI, FITC and mCherry, respectively. Ad5/3-D24-mCherry-ICOSL-CD40L internalization was evaluated alone or with melanoma chosen epitopes on a panel of melanoma cell lines at different time points (4, 8, 24, 48, 72 h) post treatment by confocal microscopy. (B) Confocal images showing the oncolytic vaccine localization in the cell 24 h post treatment.

fluorescence and morphological shifts in the cells, provide evidence of the multifaceted dynamics between the tested agents and target cells, highlighting the internalization capacity of the vaccine in tested cell lines.

3.3. Immunogenicity of tumor cell death in vitro

To evaluate whether immunogenic cell death was triggered by the treatments, the expression of specific markers, such as the exposure of calreticulin (CRT) on the cell surface, and the extracellular release of ATP release were measured on melanoma cells treated according to Table 2. Immunogenic cell death was observed when treating cells with the virus and combinatorial therapy, especially in MUG Mel-2 cells, compared to the other tested ones (Fig. 3 A-C). Therefore the obtained results suggest that MUG Mel-2 cells is the most susceptible for cell death when treated with the virus and the combinatory therapy thus, it was selected for further *in vitro* and *in vivo* studies (ATP: Ad5/3-D24-ICOSL-CD40L 75.6 % *vs* Ad5/3-D24-ICOSL-CD40L + $Q61R_{55–64}$ 74.8 %; CRT: Ad5/3-D24-ICOSL-CD40L 11.1 % *vs* Ad5/3-D24-ICOSL-CD40L + $Q61R_{55–64}$ 11.3 %) (Fig. 3D). Indeed, it is well known that adenoviruses are highly immunogenic and induce ICD [44]. While peptide-based vaccines require administration with an adjuvant to enhance immune reaction to their presence [45]. Furthermore, these findings are in line with previously reported results [28].

3.4. Efficacy studies in melanoma models

In order to test alternative melanoma therapeutic options, we firstly established 3D culture models as suitable *in vitro* tools to evaluate the anticancer efficacy of the tested agents. Therefore, aiming to mimic a hypothetical *in vivo* treatment, human 3D spheroids consisting of MUG Mel-2 cells have been formed and a long-term follow-up, which included the measurements of spheroid' integrity and growth kinetics, by registering both the areas (μm^2) and the tumor volume (mm^3), was conducted (Fig. 4 B—C). Melanoma spheroids have been treated according to the scheme presented in Table 3. The results revealed that the treatment, either with the oncolytic virus alone or in combination with melanoma specific epitope ($Q61R_{55–64}$) was able to reduce the spheroid's area and tumor volume until day 31 thus demonstrating its long-term effectiveness (spheroid's area: Ad5/3-D24-ICOSL-CD40L: 89619 μm^2 *vs* Ad5/3-D24-ICOSL-CD40L + $Q61R_{55–64}$: 110871 μm^2 tumor volume: Ad5/3-D24-ICOSL-CD40L: 0.014 mm^3 *vs* Ad5/3-D24-ICOSL-CD40L + $Q61R_{55–64}$: 0.017 mm^3) (Fig. 4 B—C). These results are not surprising since spheroids were a mono-system composed of tumoral

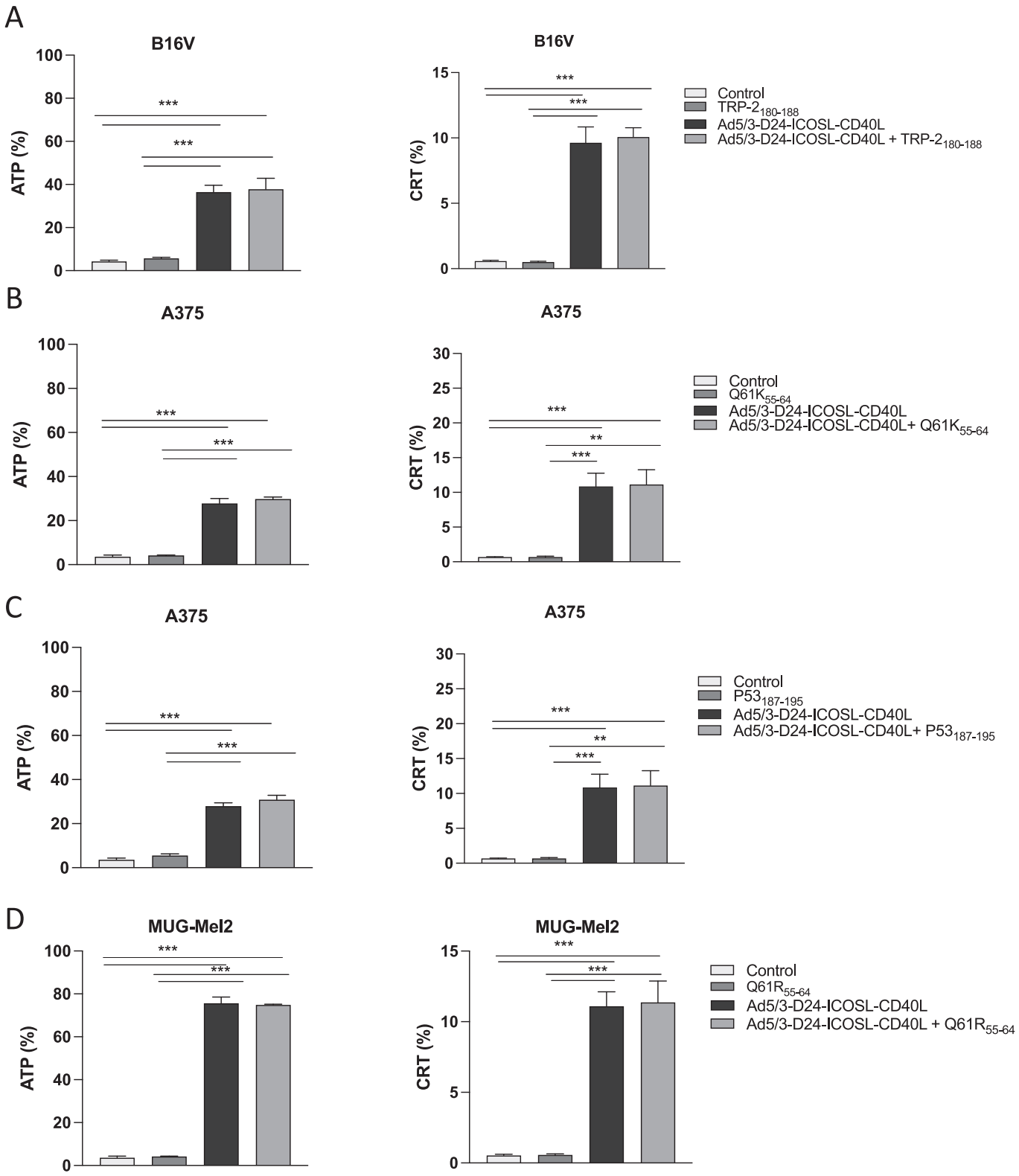

Fig. 3. Assessment of ATP release and CRT exposure. ATP levels were detected 72 h after infection with i) Ad5/3-D24-ICOSL-CD40L at 100 VP/cell, ii) selected tumoral epitopes at the concentration of 10 μg/mL of A) MUG Mel-2, B—C) A375 and D) B16V and ii) combination with the virus and peptides. Data are expressed as the % of extracellular ATP, assessed with ATP determination kit CellTiter-Glo® Luminescent Cell Viability Assay (Promega), the luminescence was then assessed with Viktor Nivo™. CRT levels were detected 48 h after infection with i) Ad5/3-D24-ICOSL-CD40L at 100 VP/cell, ii) selected tumoral epitopes at the concentration of 10 μg/mL of A) MUG Mel-2, B—C) A375 and D) B16V and ii) combination with the virus and peptides. Data are expressed as the % of positive cells for CRT, measured by flow cytometry (BD FACSAria III, Becton Dickinson, USA) followed by specific antibody staining. Statistical analysis was performed with *t*-test (**$P \leq 0.01$, ***$P \leq 0.001$).

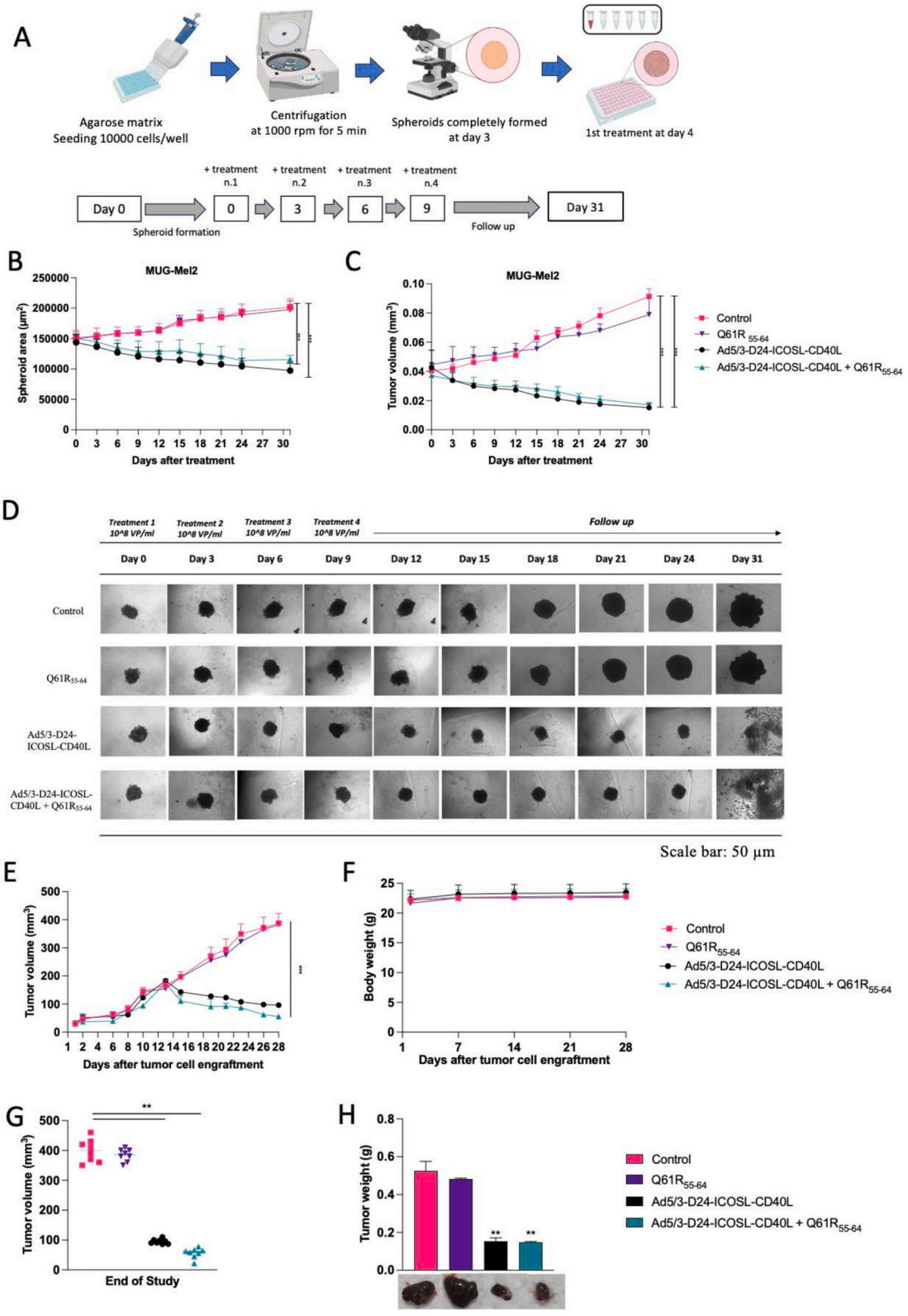

Fig. 4. Evaluation of antitumor efficacy by using 3D *in vitro* MUG Mel-2 melanoma and immunodeficient Balb/c nude mouse models. (A) Scheme of the protocol for the 3D *in vitro* spheroids on MUG Mel-2 melanoma cell line. (B) Spheroids area measured throughout the study. Spheroids were treated according to the scheme presented in Table 3. (C) Spheroids volume was assessed by the formula $0.52 \times \text{length} \times (\text{width})^2$. (D) 3D culture morphology over the time. (E) Prior to the start of treatment, tumors (MUG Mel-2) of sizes ~5 × 5 mm in diameter were randomized. Once tumors have been formed, mice were treated, intratumorally (i.t.), according to the scheme presented in Table 5. Tumor volume (mm^3) was measured throughout the experiment. (F) Body weight was measured throughout the study. (G) Tumor volume measurement was registered at the end of the study. (H) Tumor weight was assessed at the end of the study. Error bars, mean ± SEM, ** = $p \leq 0.05$, *** = $p \leq 0.0001$.

cells without immune components; thus, the peptide could not induce a cancer-specific immune response.

Furthermore, to assess the oncolytic properties of the virus, we carried out *in vivo* studies in immunodeficient xenograft melanoma MUG Mel-2 mouse model. Indeed, due to known limitations of the model, such as lack of a thymus and defected adaptive immune response, the effect of the combined treatment was not optimally determined. In fact, similar anti-cancer efficacy was observed in mice treated, intratumorally, with oncolytic adenovirus Ad5/3-D24-ICOSL-CD40L (*vs.* control, $p \leq 0.0001$, *vs.* $Q61R_{55–64}$, $p \leq 0.0001$) and combination therapy (Ad5/3-D24-ICOSL-CD40L with $Q61R_{55–64}$ *vs.* control, $p \leq 0.0001$, *vs.* $Q61R_{55–64}$ $p \leq 0.0001$) (Fig. 4E) and treatments were well tolerated thus suggesting its safety (Fig. 4F). At the end of the study, the average volume size of a tumor for mice treated with the Ad5/3-D24-ICOSL-CD40L, and the combinatory therapy was, respectively 96, and 55.5 mm^3 compared to 387.5 mm^3 (control) and 382.5 mm^3 ($Q61R_{55–64}$). Nevertheless, bearing in mind the employed model, it is important to highlight that the observed anti-tumor efficacy have not included any contribution from the hosts' adaptive immune responses therefore the peptide was not able to efficiently exert its immunomodulatory effect.

3.5. 3D Co-culture of MUG Mel-2 and PBMCs treated with the oncolytic vaccine provides synergistic anti-cancer effect

To test the proposed oncolytic vaccine in the presence of human immune components, the development of a model that could reveal insights into tumorigenesis and mimic tumor structures have been prioritized. Therefore, in order to investigate new potential treatments against melanoma and to obtain more reliable and predictable results for human application, we generated melanoma spheroids from MUG Mel-2 cells that we co-cultured with peripheral blood immune cells (PBMCs) isolated from healthy donors (Supplementary Fig. 4). PBMCs have been selected with HLA matching to the chosen melanoma cell line (A*02:03). The HLA compatibility is crucial to obtain an integrated system that should simulate the heterogeneity of the tumor microenvironment and the complex interactions between tumor cells and the immune system [46].

To establish a 3D co-culture model able to represent the immune response towards melanoma, we firstly addressed, through fluorescence microscopy, the effective infiltration of the immune cells (PBMCs) within the 3D tumor-like structure. Then, to characterize the 3D structure, we used imaging acquisition in bright field and in fluorescence (Supplementary Fig. 4) and we monitored the growth of tumor spheroids before and after the PBMCs infiltration by measuring the spheroid's areas (Supplementary Fig. 4B) (spheroid's average area at day 3: 166357 μm^2 *versus* spheroid's average area after the PMBCs addition: 234785 μm^2) thus confirming the correct integration of the immune components in the 3D culture system. Once the 3D tumor structures were assessed, we tested the antitumor immune response of Ad5/3-D24-ICOSL-CD40L, $Q61R_{55–64}$ and their combinations according to the treatment schedule presented in Table 4 and Fig. 5. Improved anticancer efficacy was observed using the virus in association with $Q61R_{55–64}$ until day 31 (Ad5/3-D24-ICOSL-CD40L + $Q61R_{55–64}$ spheroid's area: 54708 μm^2; tumor volume 0.005 mm^3) as compared to the monotherapies (Ad5/3-D24-ICOSL-CD40L spheroid's area: 76643 μm^2; tumor volume 0.008 mm^3; $Q61R_{55–64}$ spheroid's area: 868268 μm^2; tumor volume:

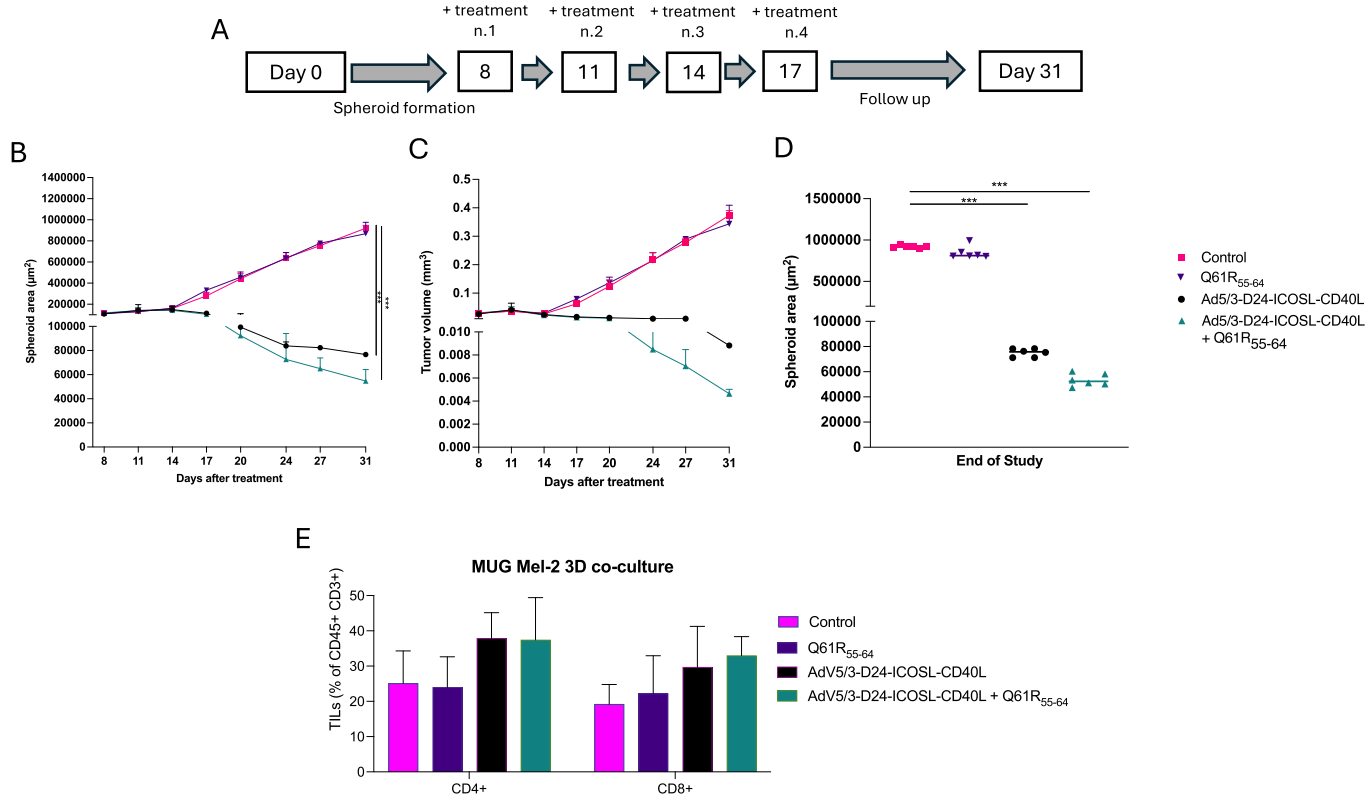

Fig. 5. Assessment of anti-cancer efficacy and immune cell infiltration of tested combinatory therapy on MUG Mel-2 3Dco-culture model. (A) MUG Mel-2 cells were seeded at a density of 7500 cells/well in 96-well and centrifuged at 1000 rpm for 5 min, to form spheroids. At day 6, PBMCs were added to the tumor spheroids in a ratio 1:4. On day 8, spheroids were treated with Ad5/3-D24-ICOSL-CD40L (10^9 VP/mL), $Q61R_{55–64}$ (10 g/mL) and their combinations as described in Table 4. Spheroids were checked under the microscope every three day. Statistical analysis was performed with *t*-test (*$P \leq 0.05$, **$P \leq 0.01$, ***$P \leq 0.001$). (B-C-D) Spheroid's size was measured on two dimensions every three days while the volume was obtained by applying the formula 0.52 × length×$(width)^2$. The area was measured using AxioVision software by Zeiss. (E) Levels of tumor infiltrating lymphocytes $CD3^+$, $CD4^+$, $CD8^+$ in MUG Mel-2 3D co-culture. Samples were acquired using BD Lyric FACS Flow. Statistical analyses were carried out with one-way ANOVA test. Error bars, mean ± SEM, ***, $p < 0.001$.

0.344 mm^3) (Fig. 5 B—D, Supplementary Fig. 5). Moreover, the combination treatment group showed a synergistic anti-tumor effect ($R > 1$) on Day 31 (Table 8) thus highlighting the clinical potential of the proposed treatment for melanoma patients.

Phenotyping analyses of TILs isolated from collected spheroids showed that the virus alone or combined with $Q61R_{55–64}$ was able to increase the level of immune cell infiltrates, especially CD8+ T cells (control: 19.17 %, Ad5/3-D24-ICOSL-CD40L: 29.67 %, $Q61R_{55–64}$: 22.23 %, combination therapy: 32.98 % and CD4+ T cells (control: 25.08 %, Ad5/3-D24-ICOSL-CD40L: 37.86 %, $Q61R_{55–64}$: 23.99 %, combination therapy: 37.41 % (Fig. 5E). Collectively, these results advocate that the adenovirus vaccine is effectively able to enhance the infiltration of both CD4+ helper and CD8+ cytotoxic T lymphocytes, and therefore exerting a central role in the spheroid volume control.

3.6. Extracellular vesicles enhance the targeted delivery of the oncolytic vaccine to the tumor

Advanced melanoma is hard to treat, moreover considering that the systemic administration is preferable for reaching metastases throughout the body, alternative approaches for the delivery of the oncolytic vaccine should be explored. Moreover, the ability of oncolytic vaccines to induce antitumor immune responses may be enhanced when administered systemically. Therefore, the possibility of adopting a delivery strategy able to ensure optimal immune responses development is a crucial challenge that must be tackled to broaden the potential applications of oncolytic vaccines in cancer therapy [48]. In response to this need, the role of EVs, which are, naturally occurring cargo-delivery agents, emerges as a potential carrier for tumor-targeted therapeutic applications [23,48]. In fact, previous studies on the delivery of OVs alone or in combination with anti-cancer agents [22,23,49] showed that OVs loaded in EVs reduced their immune recognition by neutralizing antibodies and enhance the antitumor effect. These characteristics make extracellular vesicles a promising candidate for drug delivery and can be used here as a trojan horse for the delivery of the oncolytic vaccine. The idea is to use EVs to carry immunogenic virus and tumor antigens in order to stimulate specific anticancer immune responses thus contributing to tumor growth control. Thus, herein, in the first set of experiments, we assessed whether the encapsulation of the oncolytic vaccine into the MUG Mel-2 -derived EVs had influence on the particle size distribution by using NTA (Supplementary Fig. 6A). After encapsulation, free viruses remaining in solution were chemically inactivated as previously reported [22]. Size distribution of both control EVs and EVs loaded with the oncolytic formulations were detected to be in the range of 50–250 nm. The size distribution of EV-Virus overlapped with the size of the virus with most of the EVs being in the range of the size as the virus (Supplementary Fig. 6A). The adenovirus virion has a viral structure of 90–100 nm in size packed inside the EV (Supplementary Fig. 6C), moreover the remaining free virus was routinely inactivated (please, see the procedure in the Material and Methods section) in the EV-Virus formulations before moving to the *in vivo* experiments. Further EV characterization was carried out by western blot analysis demonstrating the presence of specific EV biomarkers such as CD29, TSG101, CD81 and CD9 in all the samples (Supplementary Fig. 6B). Moreover, prior research conducted by Saari et al. [50] established the presence of adenoviral proteins (hexon) in EV-Virus formulations using western blot analysis. Specifically, hexon proteins of approximately 130 kDa and 110 kDa were identified in EV-Virus samples, demonstrating the capacity of EVs to carry adenoviral particles. However, it is important to note that the efficiency of loading EVs still requires comprehensive exploration and further study. Thus, additional research is necessary to enhance our understanding of the mechanisms involved and to optimize the loading characteristics of EVs for drug delivery applications.

Finally, cryo-EM experiments displayed the EV integrity and the possible presence of the virus inside the vesicles (Supplementary Fig. 6C). Nevertheless it should be considered that EV-virus formulation might consist of infectious adenoviral particles but also of adenoviral capsids fragments and DNA material. Moreover, a previous research paper provided detailed morphological imaging of EVs infected with an oncolytic adenovirus similar to Ad5/3-D24-ICOSL-CD40L but featuring a different transgene, GM-CSF. As described earlier the infected EVs were found to contain large membrane fragments, free virions and vesicles of various sizes [50]. Collectively, our EV-virus formulation from the immunological point of view may contribute to activation of both innate and adaptive immune responses thus enhancing the antitumor effect. Therefore such concept can work as cancer vaccine since EV does not need to contain only intact adenoviral particles in order to provide clinical efficacy.

To further investigate the internalization of the cancer vaccine into the cancer-derived EVs, confocal microscopy studies were performed on MUG Mel-2 cell line, by assessing the transfection through fluorescent protein visualization (Fig. 6). The progress of the viral infection using Ad5/3-D24-ICOSL-CD40L (expressing mCherry) could be monitored by detecting the emission signal of the protein fluorophore mCherry (excitation λ: 540–590 nm; emission λ: 550–650) which is expressed by the virus. The more intense the emission of this signal, the greater the concentration of the fluorophore, and consequently the presence of the actively replicating oncolytic virus inside tumor cells. Previous studies suggest that EVs can be internalized into target cells and deliver their cargo [51] thus, herein, indocyanine green (ICG) was used to stain EVs membrane and visualize the EV-localization into MUG Mel-2 cells (excitation λ: 789 nm; emission λ: 814 nm), while FITC signal (excitation λ: 517 nm; emission λ: 498 nm) is detected due to its conjugation to the selected melanoma epitope (FITC-$Q61R_{55–64}$). Confocal analysis revealed the uptake of EVs in MUG Mel-2 cells showing great intensity of ICG emitted by EVs which are localized in the cytoplasm, without reaching the nucleus (Fig. 6). Interestingly, to confirm the internalization of the selected melanoma epitope, $Q61R_{55–64}$, and the oncolytic adenovirus, expressing mCherry, in cancer-derived EVs, confocal microscopy images of EVs labeled with ICG and loaded with the oncolytic vaccine showed co-localization of the vaccine components within EVs. Collectively, these results suggest that EVs could deliver both the oncolytic virus and melanoma epitope into NRAS mutant melanoma cell line *in vitro*.

Next, to study the immunostimulatory functions of the oncolytic vaccine and the possibility of using EVs for its targeted delivery, a humanized xenograft melanoma MUG Mel-2 mouse model was exploited. This represents the closest alternative to the reality of a patient with NRAS mutant melanoma since it allows to study an HLA restricted T cell responses to a defined tumor antigen *in vivo*. Additionally, EVs are gaining attention as potential tool for cancer immunotherapy [52], thus current research is exploring the potential of EV-based treatments, including drug delivery and cancer vaccines. Moreover, considering that the systemic delivery may be limited when using viruses, we proposed

Table 8
Assessment of therapeutic synergy with FTV method in 3D co-culture melanoma model.

Conditions	Avg. area day 31 (μm^2)	FTV observed*	FTV expected**	Ratio (exp./obs.)
Ad5/3-D24-ICOSL-CD40L	76,643	0,08		
Ad5/3-D24-ICOSL-CD40L + $Q61R_{55–64}$	54,708	0,06	0,08	1,32
$Q61R_{55–64}$	868,268	0,9		
Control	920,158			

FTV (mean value of tumor volume experimental/mean value of tumor volume control) or (mean tumor volume experimental)/(mean tumor volume control). * (Mean FTV of experimental condition) by (mean FTV of control). **(expected FTV by the observed FTV). A ratio of >1 indicates a synergistic effect, and a ratio of <1 indicates a less than additive effect as previously reported [47].

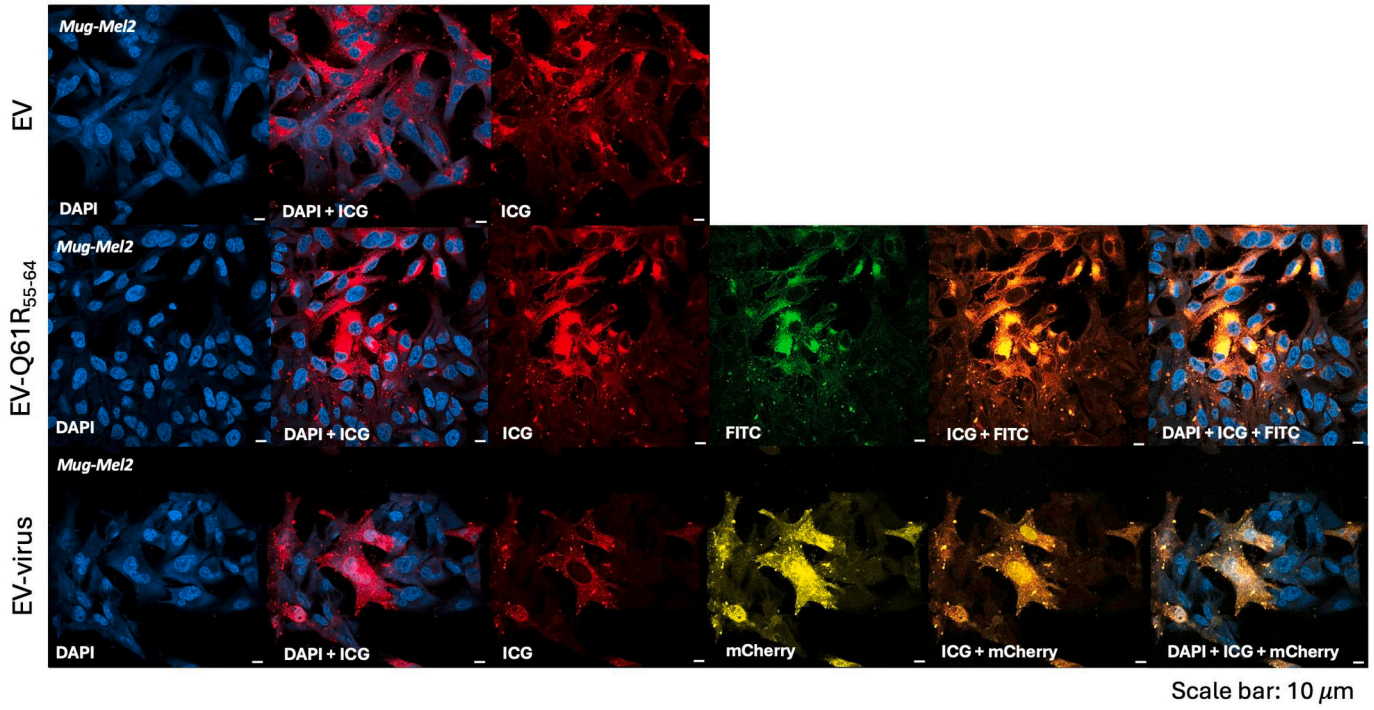

Fig. 6. Intracellular biodistribution of EVs and loaded EVs in MUG Mel-2 cells. Confocal analysis was performed by using Zeiss LSM800 equipped with 63× oil objective. MUG Mel-2 cells were analyzed post treatment with EV-Q61R$_{55–64}$, EV-Virus and EV formulations. For nuclei staining DAPI was used while FITC, ICG and mCherry were used to detect respectively the melanoma epitope Q61R$_{55–64}$, EVs and the virus. Scale bar 10 μm.

the use of the intravenous route of administration for the oncolytic vaccine based on the encapsulation into EVs. Therefore, in the *in vivo experiments* performed in humanized mice we have evaluated both the biodistribution and the anticancer efficacy of different EV-formulations delivered intravenously in a model which generates a closer representative of patients' antitumor response.

In order to have a direct evidence of the cancer specific targeting induced by melanoma derived-EVs, we labeled the formulations with near infrared (NIR) fluorescent ICG for evaluating the whole-body biodistribution of EV formulations, carrying the oncolytic vaccine (oncolytic adenovirus Ad5/3-D24-ICOSL-CD40L expressing mCherry, and FITC-Q61R$_{55–64}$), administered intravenously in NRAS mutated MUG Mel-2 humanized mice (Fig. 7). The results showed a tumor-specific fluorescent signal in mice treated with EVs formulations, which was not detected in mice administered either with ICG or FITC fluorescent dye alone (Supplementary Fig. 7). These results provide a direct demonstration of the selective tropism of EV-formulations delivering both vaccine components to the tumor. This effect was then

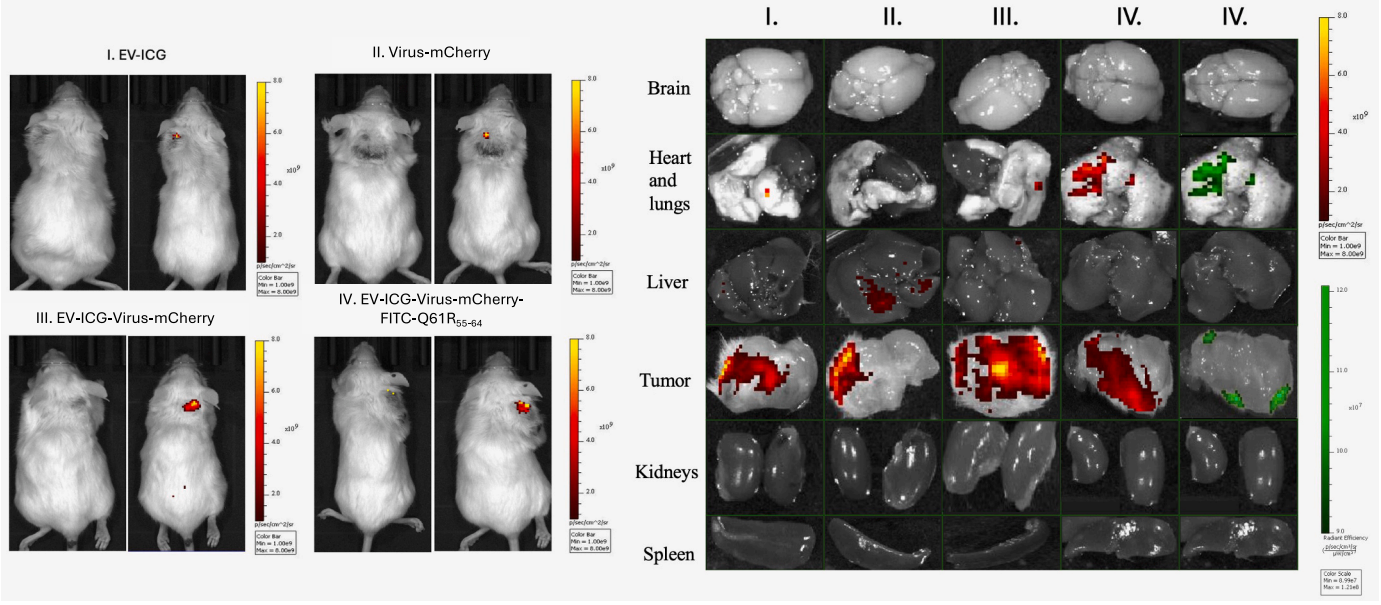

Fig. 7. Melanoma derived EV-formulations for tumor targeting. Representative images of the photon emission (fluorescence) of melanoma-derived EVs and Ad5/3-D24-ICOSL-CD40L expressing mCherry in i.v treated mice in the tumor area only. Fluorescence emitted by explanted organs from NSG mice treated with EVs formulations and adenoviral vector. Fluorescence quantified by using the Living Image Software (PerkinElmer, Waltham, MA, USA).

confirmed by *ex vivo* imaging analysis of the fluorescence emitted by the dissected organs that showed a positive signal (both coming from ICG and FITC, Fig. 7) originating selectively from the tumor of mice treated with EV-formulation delivering the oncolytic vaccine. In this context, it should be noted that a fluorescence signal was also present in the lungs of the mice treated with EV-formulations. In fact, most studies have shown that EVs predominantly accumulate in the liver, lungs, and spleen after systemic administration, with lesser accumulation in other organs such as the brain, muscle, heart, and kidneys [53]. On the other hand, Edelmann and Kima revealed that small EVs, especially those expressing tetraspanin 8, were more taken up by the pancreas and lungs and rarely by the liver and gut. This study has demonstrated that alterations in

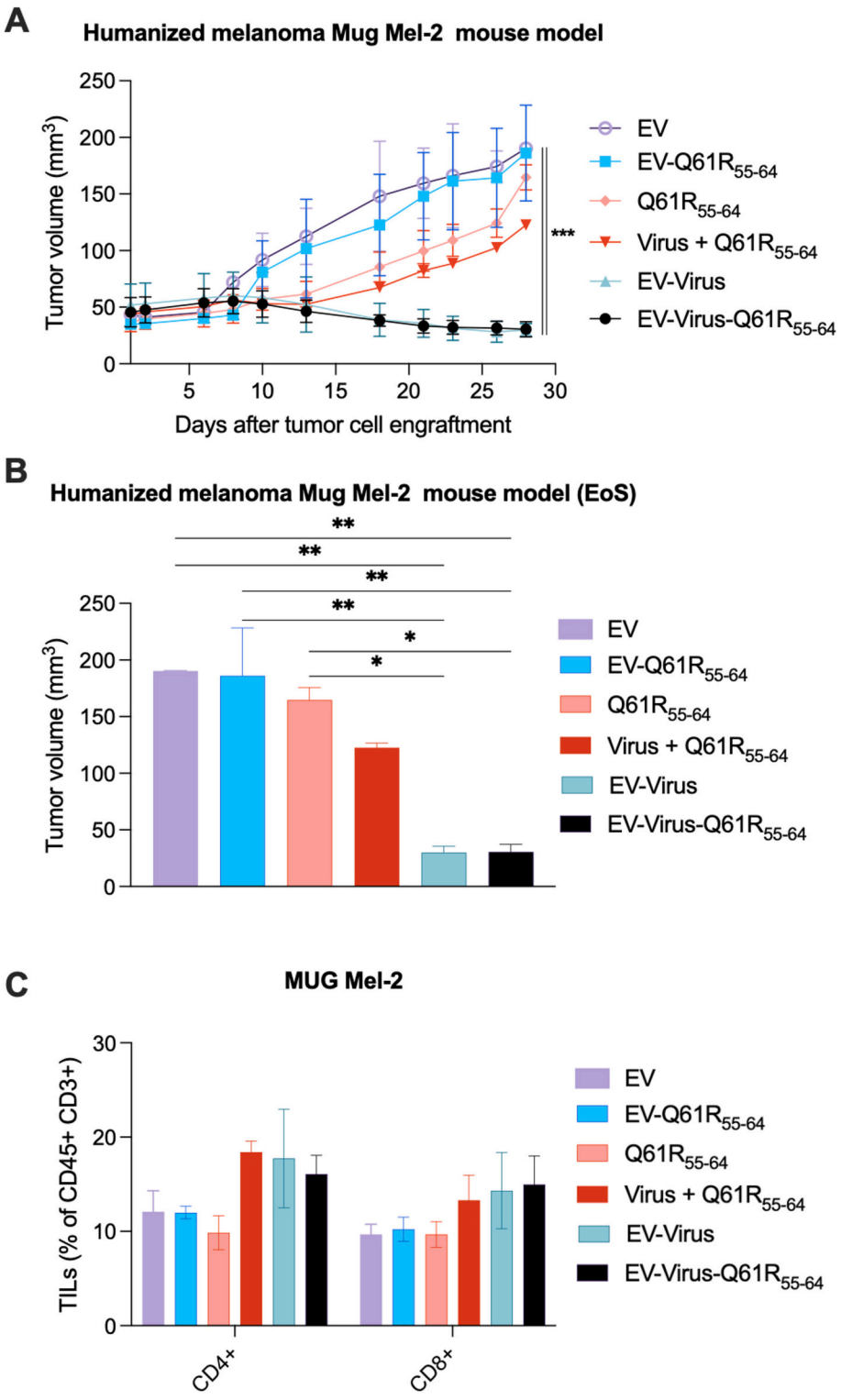

Fig. 8. Antitumor efficacy assessment of EVs, EV-Q61R$_{55–64}$, Q61R$_{55–64}$, Virus + Q61R$_{55–64}$, EV-Virus and EV-Virus-Q61R$_{55–64}$ in humanized melanoma MUG Mel-2 model. (A) Tumor volume (mm^3) measured throughout the study. (B) Tumor volume (mm^3) measured at the end of the study (Day 30). Statistical analyses were carried out with ANOVA test. Error bars, mean ± SEM, *, $p \leq 0.05$; ***, $p < 0.001$. (C) Levels of tumor infiltrating lymphocytes CD4$^+$, CD8$^+$ expression in collected tumors (end of study). Samples were acquired using BD Lyric FACS Flow.

abundance of tetraspanin on small EVs affects their tropism [54]. Therefore, taken into account these considerations, we can speculate that presence of EV-related fluorescent signal in lungs can be related with high expression level of tetraspanin 8 on the surface of EVs. Nevertheless, this will need to be further confirmed and will certainly be the subject of future investigation.

Moreover, the preferential accumulation of the dye was confirmed by confocal microscopy analysis performed on section of tumor and liver isolated from human $CD34^+$ hematopoietic stem- melanoma-engrafted NSG variant mice (Supplementary Fig. 8). Although the fluorescence intensity obtained through confocal microscopy appeared to be weaker compared to *ex vivo* imaging, it is important to consider that the latter captures all fluorescence emitted by a tissue sample, whereas confocal microscopy was utilized on extremely thin tissue slices measuring only a few microns (10 μm). This data provides additional evidence at the microscopic level supporting the EV-tumor-targeting capabilities as previously demonstrated [49].

Therapeutic efficacy has also been an integrated part of the study with the humanized MUG Mel-2 $CD34^+$ model. Improved anti-cancer efficacy was observed in mice treated with EV-Virus *versus* EV ($p \leq 0.01$) and in mice treated with EV-Virus-$Q61R_{55–64}$ *versus* EV (Fig. 8). After 28 days of treatment, the average volume size of a tumor in EV-Virus regime group was 29,84 mm^3, EV-Virus-$Q61R_{55–64}$ 30,44 mm^3 compared to EV 190 mm^3 (Fig. 8). The observed anti-cancer effect is influenced not only by the oncolyses itself but also by the anti-cancer immune responses triggered by the investigated formulations. Given that the engineered adenovirus Ad5/3-D24-ICOSL-CD40L is highly immunogenic, it is anticipated that the vector will be cleared from the body by the immune system rapidly. Therefore, the anti-cancer effect mediated solely by the virus is likely less effective than the EV formulations containing the vaccine, primarily due to reduced accumulation in the tumor tissue and more rapid systemic clearance. In addition to that, it has been previously reported that EVs can protect viruses from the host immune system [55]. All in all, we can speculate that EV formulations may improve the targeted delivery of adenoviruses to tumors while offering protection against host immune responses. Additionally, these formulations could lead to an increased viral load within the tumor tissue, which may induce immunogenic cell death and result in a more effective anti-cancer response compared to the use of viruses alone.

To be mentioned, it has been previously demonstrated that cancer derived EVs can enhance the infiltration of T cells in the tumor, therefore in the present study we performed a T-cell phenotyping analysis. The obtained results highlight enhanced infiltration of cytotoxic $CD8^+$ and $CD4^+$ T cells in mice treated with the EV-Virus ($CD8^+$: 14.31 %; $CD4^+$: 17.74 %), Virus+$Q61R_{55–64}$ ($CD8^+$: 13.31 %; $CD4^+$: 18.41 %), EV-Virus-$Q61R_{55–64}$ ($CD8^+$: 14.98 %; $CD4^+$: 16.08 %) compared to EV ($CD8^+$: 9.67 %; $CD4^+$: 12.08 %), $Q61R_{55–64}$ ($CD8^+$: 9.67 %; $CD4^+$: 9.86 %) and EV- $Q61R_{55–64}$($CD8^+$:10.23 %; $CD4^+$: 11.99 %). Taken together we can speculate that the presence of both co-stimulatory molecules, encoded by the vector contributed to enhanced infiltration of $CD8^+$, and $CD4^+$ T cells in the tumors.

4. Conclusions

In this study, we advocated EVs as a tool for systemic delivery of oncolytic vaccine for enhanced anti-cancer effect. Furthermore, we demonstrated that encapsulation into EVs does not change the ability of OVs to infect cancer cells and induce infiltration of CD4+ and CD8+ T-cells. Altogether, our studies profoundly support the systemic administration of an oncolytic vaccine using EVs as an efficacious therapeutic strategy for treating primary and metastatic melanoma. Furthermore, the tested approach can be further combined with checkpoint inhibitors to address immunosuppressive TME and to counterplay with inhibition of T cell activation.

Funding

The authors declare that the financial support was received for the research, authorship, and/or publication of this article. M.G. acknowledges the STARS Starting Grant (STARS StG) (Grant Number: GARO_STARS_MUR22_01) and PRID 2023 (GARO_BIRD23_01) funded by the University of Padua. S.S. and M.G. acknowledge the EU funding within the MUR PNRR "National Center for Gene Therapy and Drugs based on RNA Technology" (Project no. CN00000041, CN3 – Spoke #8 "Platform for DNA/RNA delivery"). L.K. was supported by the National Science Centre, Poland, SONATA (2022/47/D/NZ7/03212), The National Centre for Research and Development, Poland, LIDER (0258/L-14/2023) and the National Institute of Public Health NIH – National Research Institute, Poland (BW-3/2024).

CRediT authorship contribution statement

Sara Mathlouthi: Writing – review & editing, Investigation, Data curation. **Lukasz Kuryk:** Writing – review & editing, Writing – original draft, Visualization, Resources, Investigation, Formal analysis, Data curation, Conceptualization. **Marta Prygiel:** Writing – review & editing. **Maria Giovanna Lupo:** Writing – review & editing, Investigation. **Aleksandra Anna Zasada:** Writing – review & editing. **Cristiano Pesce:** Writing – review & editing. **Nicola Ferri:** Writing – review & editing. **Beate Rinner:** Writing – review & editing. **Stefano Salmaso:** Writing – review & editing. **Mariangela Garofalo:** Writing – review & editing, Writing – original draft, Visualization, Validation, Supervision, Resources, Project administration, Methodology, Investigation, Funding acquisition, Data curation, Conceptualization.

Declaration of competing interest

The authors declare the following financial interests/personal relationships which may be considered as potential competing interests: Author LK is an employee and/or shareholder of Valo Therapeutics. The other authors declare that the research was conducted in the absence of any commercial or financial relationship that could be construed as a potential conflict of interest.

Appendix A. Supplementary data

Supplementary data to this article can be found online at https://doi.org/10.1016/j.jconrel.2024.10.057.

Data availability

Data will be made available on request.

References

[1] M. Arnold, D. Singh, M. Laversanne, J. Vignat, S. Vaccarella, F. Meheus, A.E. Cust, E. de Vries, D.C. Whiteman, F. Bray, Global burden of cutaneous melanoma in 2020 and projections to 2040, JAMA Dermatol. 158 (2022) 495–503, https://doi.org/10.1001/jamadermatol.2022.0160.

[2] C. Garbe, U. Keim, T. Amaral, C. Berking, T.K. Eigentler, L. Flatz, Prognosis of Patients with Primary Melanoma Stage I and II According to American Joint Committee on Cancer Version 8 Validated in Two Independent Cohorts: Implications for Adjuvant Treatment 40, 2024, https://doi.org/10.1200/JCO.22.00202 (n.d.).

[3] A. Boespflug, J. Caramel, S. Dalle, L. Thomas, Treatment of NRAS-mutated advanced or metastatic melanoma: rationale, current trials and evidence to date, Ther. Adv. Med. Oncol. 9 (2017) 481–492, https://doi.org/10.1177/1758834017708160.

[4] H.J. Kim, Y.H. Kim, Molecular Frontiers in melanoma: pathogenesis, diagnosis, and therapeutic advances, Int. J. Mol. Sci. 25 (2024), https://doi.org/10.3390/ijms25052984.

[5] F.C. Kelleher, G.A. McArthur, Targeting NRAS in melanoma, Cancer J. 18 (2012). https://journals.lww.com/journalppo/fulltext/2012/03000/targeting_nras_in_melanoma.4.aspx.

[6] W. Wagstaff, R.N. Mwamba, K. Grullon, M. Armstrong, P. Zhao, B. Hendren-Santiago, K.H. Qin, A.J. Li, D.A. Hu, A. Youssef, R.R. Reid, H.H. Luu, L. Shen, T.-

C. He, R.C. Haydon, Melanoma: molecular genetics, metastasis, targeted therapies, immunotherapies, and therapeutic resistance, Genes Dis. 9 (2022) 1608–1623, https://doi.org/10.1016/j.gendis.2022.04.004.
[7] P. Mohite, V. Yadav, R. Pandhare, S. Maitra, F.M. Saleh, R.M. Saleem, H.S. Almalky, V. Kumarasamy, V. Subramaniyan, M.M. Abdel-Daim, D.E. Uti, Revolutionizing cancer treatment: unleashing the power of viral vaccines, monoclonal antibodies, and proteolysis-targeting chimeras in the new era of immunotherapy, ACS Omega 9 (2024) 7277–7295, https://doi.org/10.1021/acsomega.3c06501.
[8] J. Liu, M. Fu, M. Wang, D. Wan, Y. Wei, X. Wei, Cancer vaccines as promising immuno - therapeutics: platforms and current progress, J. Hematol. Oncol. (2022) 1–26, https://doi.org/10.1186/s13045-022-01247-x.
[9] W. Liu, H. Tang, L. Li, X. Wang, Z. Yu, J. Li, Peptide-based therapeutic cancer vaccine: current trends in clinical application, Cell Prolif. 54 (2021) e13025, https://doi.org/10.1111/cpr.13025.
[10] Y.L. Vishweshwaraiah, N.V. Dokholyan, mRNA vaccines for cancer immunotherapy, Front. Immunol. 13 (2022), https://doi.org/10.3389/fimmu.2022.1029069.
[11] L.-J. Duan, Q. Wang, C. Zhang, D.-X. Yang, X.-Y. Zhang, Potentialities and challenges of mRNA vaccine in Cancer immunotherapy, Front. Immunol. 13 (2022), https://doi.org/10.3389/fimmu.2022.923647.
[12] S.Y. Lim, E. Shklovskaya, J.H. Lee, B. Pedersen, A. Stewart, Z. Ming, M. Irvine, B. Shivalingam, R.P.M. Saw, A.M. Menzies, M.S. Carlino, R.A. Scolyer, G.V. Long, H. Rizos, The molecular and functional landscape of resistance to immune checkpoint blockade in melanoma, Nat. Commun. 14 (2023) 1516, https://doi.org/10.1038/s41467-023-36979-y.
[13] O. Hemminki, J.M. dos Santos, A. Hemminki, Oncolytic viruses for cancer immunotherapy, J. Hematol. Oncol. 13 (2020) 84, https://doi.org/10.1186/s13045-020-00922-1.
[14] M.M. Rahman, G. McFadden, Oncolytic viruses: newest frontier for cancer immunotherapy, Cancers (Basel) 13 (2021), https://doi.org/10.3390/cancers13215452.
[15] E. Kelly, S.J. Russell, History of oncolytic viruses: genesis to genetic engineering, Mol. Ther. 15 (2007) 651–659, https://doi.org/10.1038/sj.mt.6300108.
[16] S.J. Russell, G.N. Barber, Oncolytic viruses as antigen-agnostic cancer vaccines, Cancer Cell 33 (2018) 599–605, https://doi.org/10.1016/j.ccell.2018.03.011.
[17] D.L. Bartlett, Z. Liu, M. Sathaiah, R. Ravindranathan, Z. Guo, Y. He, Z.S. Guo, Oncolytic viruses as therapeutic cancer vaccines, Mol. Cancer 12 (2013) 103, https://doi.org/10.1186/1476-4598-12-103.
[18] H.H. Wong, N.R. Lemoine, Y. Wang, Oncolytic viruses for cancer therapy: overcoming the obstacles, Viruses 2 (2010) 78–106, https://doi.org/10.3390/v2010078.
[19] L. Chen, M. Zuo, Q. Zhou, Y. Wang, Oncolytic virotherapy in cancer treatment: challenges and optimization prospects, Front. Immunol. 14 (2023), https://doi.org/10.3389/fimmu.2023.1308890.
[20] D.G. Roy, K. Geoffroy, M. Marguerie, S.T. Khan, N.T. Martin, J. Kmiecik, D. Bobbala, A.S. Aitken, C.T. de Souza, K.B. Stephenson, B.D. Lichty, R.C. Auer, D. F. Stojdl, J.C. Bell, M.-C. Bourgeois-Daigneault, Adjuvant oncolytic virotherapy for personalized anti-cancer vaccination, Nat. Commun. 12 (2021) 2626, https://doi.org/10.1038/s41467-021-22929-z.
[21] D.K. Jeppesen, Q. Zhang, J.L. Franklin, R.J. Coffey, Extracellular vesicles and nanoparticles: emerging complexities, Trends Cell Biol. 33 (2023) 667–681, https://doi.org/10.1016/j.tcb.2023.01.002.
[22] M. Garofalo, H. Saari, P. Somersalo, D. Crescenti, L. Kuryk, L. Aksela, C. Capasso, M. Madetoja, K. Koskinen, T. Oksanen, A. Mäkitie, M. Jalasvuori, V. Cerullo, P. Ciana, M. Yliperttula, Antitumor effect of oncolytic virus and paclitaxel encapsulated in extracellular vesicles for lung cancer treatment, J. Control. Release 283 (2018) 223–234, https://doi.org/10.1016/j.jconrel.2018.05.015.
[23] M. Garofalo, A. Villa, N. Rizzi, L. Kuryk, B. Rinner, V. Cerullo, M. Yliperttula, Extracellular vesicles enhance the targeted delivery of immunogenic oncolytic adenovirus and paclitaxel in immunocompetent mice, J. Control. Release 294 (2019) 165–175, https://doi.org/10.1016/j.jconrel.2018.12.022.
[24] M. Garofalo, A. Villa, N. Rizzi, L. Kuryk, V. Mazzaferro, P. Ciana, Systemic administration and targeted delivery of immunogenic oncolytic adenovirus encapsulated in extracellular vesicles for cancer therapies, Viruses 10 (2018) 558, https://doi.org/10.3390/v10100558.
[25] M.K. Jayasinghe, M. Pirisinu, Y. Yang, B. Peng, T.T. Pham, C.Y. Lee, M. Tan, L. T. Vu, X.T.T. Dang, T.C. Pham, H. Chen, A.Y.H. Leung, W.C. Cho, J. Shi, M.T.N. Le, Surface-engineered extracellular vesicles for targeted delivery of therapeutic RNAs and peptides for cancer therapy, Theranostics 12 (2022) 3288–3315, https://doi.org/10.7150/thno.68667.
[26] M. Garofalo, K.W. Pancer, M. Wieczorek, M. Staniszewska, S. Salmaso, P. Caliceti, L. Kuryk, From immunosuppression to immunomodulation - turning cold tumours into hot, J. Cancer 13 (2022) 2884–2892, https://doi.org/10.7150/jca.71992.
[27] L. Kuryk, S. Mathlouthi, M. Wieczorek, B. Gad, B. Rinner, A. Malfanti, F. Mastrotto, S. Salmaso, P. Caliceti, M. Garofalo, Priming with oncolytic adenovirus followed by anti-PD-1 and paclitaxel treatment leads to improved anti-cancer efficacy in the 3D TNBC model, Eur. J. Pharm. Biopharm. 199 (2024) 114300, https://doi.org/10.1016/j.ejpb.2024.114300.
[28] M. Garofalo, L. Bertinato, M. Staniszewska, M. Wieczorek, S. Salmaso, S. Schrom, B. Rinner, K.W. Pancer, L. Kuryk, Combination Therapy of Novel Oncolytic Adenovirus with Anti-PD1 Resulted in Enhanced Anti-Cancer Effect in Syngeneic Immunocompetent Melanoma Mouse Model, 2021, pp. 1–22.
[29] M. Garofalo, M. Wieczorek, I. Anders, M. Staniszewska, M. Lazniewski, M. Prygiel, A.A. Zasada, T. Szczepińska, D. Plewczynski, S. Salmaso, P. Caliceti, V. Cerullo, R. Alemany, B. Rinner, K. Pancer, L. Kuryk, Novel combinatorial therapy of oncolytic adenovirus AdV5/3-D24-ICOSL-CD40L with anti PD-1 exhibits enhanced anti-cancer efficacy through promotion of intratumoral T-cell infiltration and modulation of tumour microenvironment in mesothelioma mouse model, Front. Oncol. 13 (2023), https://doi.org/10.3389/fonc.2023.1259314.
[30] Z. Hélias-Rodzewicz, E. Funck-Brentano, N. Terrones, A. Beauchet, U. Zimmermann, C. Marin, P. Saiag, J.-F. Emile, Variation of mutant allele frequency in NRAS Q61 mutated melanomas, BMC Dermatol. 17 (2017) 9, https://doi.org/10.1186/s12895-017-0061-x.
[31] P. Koelblinger, R. Dummer, Targeted Treatment of Advanced NRAS-Mutated Melanoma 8, 2017, pp. 84616–84617.
[32] M. Maio, Melanoma as a model tumour for immuno-oncology, Ann. Oncol. 23 (2012), https://doi.org/10.1093/annonc/mds257 viii10–viii14.
[33] E. Levchenko, V.C. Sileni, J. Schachter, C. Garbe, I. Bondarenko, H. Gogas, M. Mandalá, J.B.A.G. Haanen, C. Lebbé, A. Mackiewicz, M. Tan, E. Gasal, M. Voi, D. Schadendorf, G.V. Long, Five-Year Outcomes with Dabrafenib plus Trametinib in Metastatic Melanoma, 2019, https://doi.org/10.1056/NEJMoa1904059.
[34] N.E. Thomas, S.N. Edmiston, A. Alexander, P.A. Groben, E. Parrish, A. Kricker, B. K. Armstrong, H. Anton-Culver, S.B. Gruber, L. From, K.J. Busam, H. Hao, I. Orlow, P.A. Kanetsky, L. Luo, A.S. Reiner, S. Paine, J.S. Frank, J.I. Bramson, L.D. Marrett, R.P. Gallagher, R. Zanetti, S. Rosso, T. Dwyer, A.E. Cust, D.W. Ollila, C.B. Begg, M. Berwick, K. Conway, G.E.M.S. Group, Association between NRAS and BRAF mutational status and melanoma-specific survival among patients with higher-risk primary melanoma, JAMA Oncol. 1 (2015) 359–368, https://doi.org/10.1001/jamaoncol.2015.0493.
[35] X. Wei, Z. Zou, W. Zhang, M. Fang, X. Zhang, Z. Luo, J. Chen, G. Huang, P. Zhang, Y. Cheng, J. Liu, J. Liu, J. Zhang, D. Wu, Y. Chen, X. Ma, H. Pan, R. Jiang, X. Liu, X. Ren, H. Tian, Z. Jia, J. Guo, L. Si, A phase II study of efficacy and safety of the MEK inhibitor tunlametinib in patients with advanced NRAS-mutant melanoma, Eur. J. Cancer 202 (2024) 114008, https://doi.org/10.1016/j.ejca.2024.114008.
[36] T. Randic, S. Magni, D. Philippidou, C. Margue, K. Grzyb, J.R. Preis, J. P. Wroblewska, P.V. Nazarov, M. Mittelbronn, K.B.M. Frauenknecht, A. Skupin, S. Kreis, Single-cell transcriptomics of NRAS-mutated melanoma transitioning to drug resistance reveals P2RX7 as an indicator of early drug response, Cell Rep. 42 (2023) 112696, https://doi.org/10.1016/j.celrep.2023.112696.
[37] M. Skwarczynski, I. Toth, Peptide-based synthetic vaccines, Chem. Sci. 7 (2016) 842–854, https://doi.org/10.1039/C5SC03892H.
[38] T. Kessler, W. Wick, Oncolytic virotherapy: potentially a game-changing tumor treatment, Cancer Cell 39 (2021) 753–755, https://doi.org/10.1016/j.ccell.2021.05.014.
[39] J. Yin, J.M. Markert, J.W. Leavenworth, Modulation of the intratumoral immune landscape by oncolytic herpes simplex virus virotherapy, Front. Oncol. 7 (2017), https://doi.org/10.3389/fonc.2017.00136.
[40] C. Capasso, M. Hirvinen, M. Garofalo, D. Romaniuk, L. Kuryk, T. Sarvela, A. Vitale, M. Antopolsky, A. Magarkar, T. Viitala, T. Suutari, A. Bunker, M. Yliperttula, A. Urtti, V. Cerullo, Oncolytic adenoviruses coated with MHC-I tumor epitopes increase the antitumor immunity and efficacy against melanoma, Oncoimmunology 5 (2016) 1–11, https://doi.org/10.1080/2162402X.2015.1105429.
[41] A.J. Stephens, N.A. Burgess-Brown, S. Jiang, Beyond just peptide antigens: the complex world of peptide-based cancer vaccines, Front. Immunol. 12 (2021), https://doi.org/10.3389/fimmu.2021.696791.
[42] A. Nelde, H.-G. Rammensee, J.S. Walz, The peptide vaccine of the future, Mol. Cell. Proteomics 20 (2021) 100022, https://doi.org/10.1074/mcp.R120.002309.
[43] L. Kuryk, A.W. Møller, Chimeric oncolytic Ad5/3 virus replicates and lyses ovarian cancer cells through desmoglein-2 cell entry receptor, J. Med. Virol. 92 (2020) 1309–1315, https://doi.org/10.1002/jmv.25677.
[44] J. Ma, M. Ramachandran, C. Jin, C. Quijano-Rubio, M. Martikainen, D. Yu, M. Essand, Characterization of virus-mediated immunogenic cancer cell death and the consequences for oncolytic virus-based immunotherapy of cancer, Cell Death Dis. 11 (2020) 48, https://doi.org/10.1038/s41419-020-2236-3.
[45] R.J. Malonis, J.R. Lai, O. Vergnolle, Peptide-based vaccines: current progress and future challenges, Chem. Rev. 120 (2020) 3210–3229, https://doi.org/10.1021/acs.chemrev.9b00472.
[46] D. Nagorsen, E. Thiel, HLA typing demands for peptide-based anti-cancer vaccine, Cancer Immunol. Immunother. 57 (2008) 1903–1910, https://doi.org/10.1007/s00262-008-0493-6.
[47] L. Kuryk, E. Haavisto, M. Garofalo, C. Capasso, M. Hirvinen, S. Pesonen, T. Ranki, L. Vassilev, V. Cerullo, Synergistic anti-tumor efficacy of immunogenic adenovirus ONCOS-102 (Ad5/3-D24-GM-CSF) and standard of care chemotherapy in preclinical mesothelioma model, Int. J. Cancer 139 (2016) 1883–1893, https://doi.org/10.1002/ijc.30228.
[48] B. Taheri, Z. Zarei-Behjani, A. Babaei, F.M. Moradkhan, Extracellular vesicles: a Trojan horse delivery method for systemic administration of oncolytic viruses, Regen. Eng. Transl. Med. 9 (2023) 447–457, https://doi.org/10.1007/s40883-023-00295-0.
[49] M. Garofalo, A. Villa, D. Crescenti, M. Marzagalli, L. Kuryk, P. Limonta, V. Mazzaferro, P. Ciana, Heterologous and cross-species tropism of cancer- derived extracellular vesicles 9 (2019), https://doi.org/10.7150/thno.34824.
[50] H. Saari, T. Turunen, A. Lõhmus, M. Turunen, M. Jalasvuori, S.J. Butcher, S. Ylä-Herttuala, T. Viitala, V. Cerullo, P.R.M. Siljander, M. Yliperttula, Extracellular vesicles provide a capsid-free vector for oncolytic adenoviral DNA delivery, J. Extracell. Vesicles 9 (2020) 1747206, https://doi.org/10.1080/20013078.2020.1747206.
[51] L.A. Mulcahy, R.C. Pink, D.R.F. Carter, Routes and mechanisms of extracellular vesicle uptake, J. Extracell. Vesicles 3 (2014) 24641, https://doi.org/10.3402/jev.v3.24641.

[52] C. Lyu, H. Sun, Z. Sun, Y. Liu, Q. Wang, Roles of exosomes in immunotherapy for solid cancers, Cell Death Dis. 15 (2024) 106, https://doi.org/10.1038/s41419-024-06494-z.
[53] M. Kang, V. Jordan, C. Blenkiron, L.W. Chamley, Biodistribution of extracellular vesicles following administration into animals: a systematic review, J. Extracell. Vesicles 10 (2021) e12085, https://doi.org/10.1002/jev2.12085.
[54] M.J. Edelmann, P.E. Kima, Current Understanding of Extracellular Vesicle Homing / Tropism, 2022, https://doi.org/10.15212/ZOONOSES-2022-0004.
[55] W. Ting, F. Liurong, Z. Fuwei, W. Dang, X. Shaobo, Exosomes mediate intercellular transmission of porcine reproductive and respiratory syndrome virus, J. Virol. 92 (2018), https://doi.org/10.1128/jvi.01734-17.